



ARL-TR-8595 • DEC 2018



# Synthetic Aperture Radar for Helicopter Landing in Degraded Visual Environments

by Traian Dogaru

Approved for public release; distribution unlimited.

## **NOTICES**

### **Disclaimers**

The findings in this report are not to be construed as an official Department of the Army position unless so designated by other authorized documents.

Citation of manufacturer's or trade names does not constitute an official endorsement or approval of the use thereof.

Destroy this report when it is no longer needed. Do not return it to the originator.



# **Synthetic Aperture Radar for Helicopter Landing in Degraded Visual Environments**

**by Traian Dogaru**

*Sensors and Electron Devices Directorate, ARL*

**REPORT DOCUMENTATION PAGE**

*Form Approved  
OMB No. 0704-0188*

Public reporting burden for this collection of information is estimated to average 1 hour per response, including the time for reviewing instructions, searching existing data sources, gathering and maintaining the data needed, and completing and reviewing the collection information. Send comments regarding this burden estimate or any other aspect of this collection of information, including suggestions for reducing the burden, to Department of Defense, Washington Headquarters Services, Directorate for Information Operations and Reports (0704-0188), 1215 Jefferson Davis Highway, Suite 1204, Arlington, VA 22202-4302. Respondents should be aware that notwithstanding any other provision of law, no person shall be subject to any penalty for failing to comply with a collection of information if it does not display a currently valid OMB control number.

**PLEASE DO NOT RETURN YOUR FORM TO THE ABOVE ADDRESS.**

<b>1. REPORT DATE (DD-MM-YYYY)</b> December 2018			<b>2. REPORT TYPE</b> Technical Report		<b>3. DATES COVERED (From - To)</b> May–August 2018	
<b>4. TITLE AND SUBTITLE</b> Synthetic Aperture Radar for Helicopter Landing in Degraded Visual Environments					<b>5a. CONTRACT NUMBER</b>	
					<b>5b. GRANT NUMBER</b>	
					<b>5c. PROGRAM ELEMENT NUMBER</b>	
<b>6. AUTHOR(S)</b> Traian Dogaru					<b>5d. PROJECT NUMBER</b>	
					<b>5e. TASK NUMBER</b>	
					<b>5f. WORK UNIT NUMBER</b>	
<b>7. PERFORMING ORGANIZATION NAME(S) AND ADDRESS(ES)</b> US Army Research Laboratory ATTN: RDRL-SER-U 2800 Powder Mill Road Adelphi, MD 20783-1138					<b>8. PERFORMING ORGANIZATION REPORT NUMBER</b>  ARL-TR-8595	
<b>9. SPONSORING/MONITORING AGENCY NAME(S) AND ADDRESS(ES)</b>					<b>10. SPONSOR/MONITOR'S ACRONYM(S)</b>	
					<b>11. SPONSOR/MONITOR'S REPORT NUMBER(S)</b>	
<b>12. DISTRIBUTION/AVAILABILITY STATEMENT</b> Approved for public release; distribution unlimited.						
<b>13. SUPPLEMENTARY NOTES</b>						
<b>14. ABSTRACT</b> This report analyzes the forward-looking synthetic aperture radar (SAR) system for helicopter landing assistance in degraded visual environments, currently under design at the US Army Research Laboratory. The main focus of the investigation is on SAR imaging and antenna array processing techniques. In particular, the system's point spread function is analyzed in detail by quantifying the main performance metrics: resolution, sidelobes, and grating lobes. Analytic and numeric results are illustrated with 3-D graphics. Tradeoffs and performance improvement methods are discussed. Additionally, we review several options for antenna array design and undertake a sensitivity study of the 3-D SAR image quality with respect to platform positioning errors. A design case study is presented as well, emphasizing aspects such as radar waveforms, timing, and power requirements.						
<b>15. SUBJECT TERMS</b> synthetic aperture radar, SAR, forward-looking radar, antenna array processing, degraded visual environment						
<b>16. SECURITY CLASSIFICATION OF:</b>			<b>17. LIMITATION OF ABSTRACT</b>  UU	<b>18. NUMBER OF PAGES</b>  72	<b>19a. NAME OF RESPONSIBLE PERSON</b> Traian Dogaru	
<b>a. REPORT</b> Unclassified	<b>b. ABSTRACT</b> Unclassified	<b>c. THIS PAGE</b> Unclassified			<b>19b. TELEPHONE NUMBER (Include area code)</b> (301) 394-1482	

## Contents

---

<b>List of Figures</b>	<b>iv</b>
<b>List of Tables</b>	<b>vi</b>
<b>1. Introduction</b>	<b>1</b>
<b>2. Problem Formulation and Methodology</b>	<b>2</b>
<b>3. Image Resolution, Sidelobes, and Grating Lobes</b>	<b>6</b>
3.1 Analytic Expression of the PSF and Resolution	6
3.2 Numeric Examples of PSF	13
3.3 Sidelobe and Grating Lobe Analysis	20
3.4 Imaging Performance Levers and Tradeoffs	25
3.5 Effect of Along-Track Integration on Grating Lobes	27
3.6 RSM Technique for Sidelobe Suppression	32
<b>4. Antenna Array Configurations and Scanning Techniques</b>	<b>36</b>
<b>5. Positioning Errors and Motion Compensation</b>	<b>43</b>
<b>6. System Design: Waveforms, Timing, and Power</b>	<b>50</b>
<b>7. Conclusions</b>	<b>54</b>
<b>8. References</b>	<b>57</b>
<b>List of Symbols, Abbreviations, and Acronyms</b>	<b>59</b>
<b>Distribution List</b>	<b>61</b>

## List of Figures

---

Fig. 1	Schematic representation of the helicopter-borne radar system operating as FLSAR, showing the relevant sensing geometry from a) top view and b) side view. The small antenna diagrams mark the aperture sample positions. (Drawing not to scale.).....	3
Fig. 2	Schematic representation of the helicopter-borne radar system operating as FLSAR, showing additional geometry elements not included in Fig. 1: a) top view and b) side view. (Drawing not to scale.) .....	8
Fig. 3	Graphic representation of the PSF for the radar system parameters considered in this section, with the point target placed in the origin of the coordinate system: a) x-y and y-z planes, perspective view; b) x-y and x-z planes, perspective view; c) x-y plane; d) y-z plane; e) x-z plane; f) cut along the x axis; g) cut along the y axis; and h) cut along the z axis. A Hanning window is applied to the radar data in the frequency dimension only. The color bar for the pseudo-color plots represents magnitude in decibels. ....	16
Fig. 4	Graphic representation of the PSF for the radar system parameters considered in this section, with the point target placed in the origin of the coordinate system: a) x-y and y-z planes, perspective view; b) x-y and x-z planes, perspective view; c) x-y plane; d) y-z plane; e) x-z plane; f) cut along the x axis; g) cut along the y axis; and h) cut along the z axis. For this numerical example, the radar data was tapered in all three dimensions using Hanning windows. ....	17
Fig. 5	Graphic representation of the PSF for the radar system parameters considered in this section, with the point target placed at $x_0 = 0$ , $y_0 = 8$ m, and $z_0 = 0$ : a) x-y and y-z planes, perspective view; b) x-y and y = 8 m planes, perspective view; c) x-y plane; d) y-z plane; e) y = 8 m plane; and f) cut along the y axis .....	18
Fig. 6	Graphic representation of the PSF for the radar system parameters considered in this section, with the point target placed at $x_0 = 0$ , $y_0 = 0$ , and $z_0 = 12$ m: a) z = 12 m and y-z planes, perspective view; b) z = 12 m and x-z planes, perspective view; c) x-z plane; d) y-z plane; e) z = 12 m plane; and f) cut along the z axis .....	20
Fig. 7	3-D representation of the PSF obtained with the FLSAR system “painted” on the surface of the sphere described by Eq. 21: a) perspective view and b) view along the x axis .....	21
Fig. 8	Close-up 3-D representation of the PSF obtained with the FLSAR system “painted” on the surface of the sphere described by Eq. 21: a) perspective view and b) view along the x axis .....	22
Fig. 9	Voxel magnitude along the sidelobe lines passing through the origin (or target location), evaluated on the circles a) in the y-z plane (described by Eq. 22) and b) in the x-z plane (described by Eq. 24)..	24

Fig. 10	a) Sidelobe circles in the $y-z$ plane obtained for various values of $y_c$ , and b) voxel magnitude along two of these circles, emphasizing the sidelobes (blue line) and the grating lobes (red line).....	24
Fig. 11	Graphic representation of the PSF for a fixed antenna array, with the point target placed in the origin of the coordinate system: a) $x-y$ and $y-z$ planes, perspective view; b) painted on the surface of the sidelobe sphere; c) $x-y$ plane; and d) $y-z$ plane.....	28
Fig. 12	Magnitude of the image voxels along the sidelobe lines for various numbers of along-track synthetic aperture samples, showing the variation of the first-order grating lobes for abscissa equal to $\pm 18$ m.	29
Fig. 13	Magnitude of the image voxels along the sidelobe lines for different synthetic aperture lengths, showing the variation of the first-order grating lobes for abscissa equal to $\pm 18$ m.....	30
Fig. 14	Magnitude of the image voxels along the sidelobe lines for various numbers of along-track synthetic aperture samples, showing the variation of the close-in sidelobes.....	31
Fig. 15	Representation of the 2-D aperture sample locations in the horizontal plane: a) the full set of samples and b) a random subset of those samples (80% of the original). Note that the figure is not to scale; its only purpose is to illustrate the principle of the RSM algorithm.....	33
Fig. 16	Graphic representation of the PSF for the same FLSAR parameters as in Fig. 3, after applying the RSM algorithm: a) $x-y$ and $y-z$ planes, perspective view; b) $x-y$ and $x-z$ planes, perspective view; c) $x-y$ plane; and d) $y-z$ plane.....	34
Fig. 17	Voxel magnitude along the sidelobe line, comparing the original SAR imaging algorithm with the RSM algorithm for various data percentages retained at each iteration. In all cases, the RSM procedure uses 40 iterations.....	35
Fig. 18	Voxel magnitude along the sidelobe line, comparing the original SAR imaging algorithm with the RSM algorithm for numbers of iterations. In all cases, the RSM procedure uses 90% of the data at each iteration. ....	35
Fig. 19	Schematic representation of Configuration 1 for the antenna array, showing the Tx antenna beams in pink and the Rx antenna beams in purple .....	37
Fig. 20	Schematic representation of Configuration 2 for the antenna array, showing the Tx antenna beams in pink and the Rx antenna beams in purple .....	38
Fig. 21	Schematic representation of Configuration 4 for the antenna array, showing the equivalent Tx beams in pink and the equivalent Rx beams in purple .....	39
Fig. 22	Schematic representation of Configuration 5 for the antenna array, showing the Tx–Rx beam pairs in different colors, corresponding to the waveforms transmitted on each channel .....	41

Fig. 23	Graphic representation of the PSF with the point target placed in the coordinate system origin, after introducing a set of uncorrelated positioning errors in the x direction, with standard deviation of 1 mm: a) x-y and y-z planes, perspective view; b) x-y and x-z planes, perspective view; c) x-y plane; d) y-z plane; e) x-z plane; f) cut along the x axis; g) cut along the y axis; and h) cut along the z axis.....	45
Fig. 24	Possible rotorcraft rotational errors: a) yaw of angle $\alpha$ , b) roll of angle $\beta$ , and c) pitch of angle $\gamma$ .....	46
Fig. 25	Variation of the PSF peak magnitude with the RMS of the translational errors in the three Cartesian directions: a) the monostatic antenna array described as Configuration 1 in Section 4 and b) the slightly bistatic antenna array described as Configuration 2 in Section 4.....	48

## List of Tables

---

Table 1	Comparison of various performance metrics for the five antenna array configurations considered in this section.....	42
---------	---	----

## 1. Introduction

---

The development of sensors to assist helicopter landing in degraded visual environments (DVEs) is currently an important US Army requirement addressing the Survivability of Future Vertical Lift Platforms program, one of the Army's modernization priorities. Over the past three decades, dozens of rotary-wing aircraft crashes have been responsible for a large number of casualties to US and coalition forces in different parts of the world. Out of these crashes, at least 75% have occurred in brownout conditions, where dirt or dust is stirred up and recirculated by the rotor blades, creating low- or zero-visibility environments for the pilots.<sup>1</sup> Research and development efforts to mitigate this issue starting in the early 2000s recommended several possible solutions based on optical, IR, and radar sensors.<sup>2</sup> Unfortunately, most of these solutions have proven to be either ineffective or involved unacceptable size, weight, power, and/or cost (SWAP-C), leaving the Army with a capability gap to be filled.

The US Army Research Laboratory (ARL) is currently working on a sensor solution to this problem based on millimeter-wave (MMW) imaging radar technology. The main idea behind this sensor is to combine a linear antenna array with the radar platform motion to obtain a high-resolution 3-D terrain map of the landing zone. This information would be passed to the pilot via helmet-mounted display to assist in deciding whether the landing zone is safe. Several previous efforts in developing similar sensors, based on passive or active MMW technology, have focused heavily on 2-D antenna arrays working in scanning mode to obtain a terrain map.<sup>3,4</sup> These efforts generally produced devices that proved either too expensive, unreliable, and/or inaccurate for the required task. The ARL-proposed solution leverages advanced radar imaging methodology, together with the current boom in commercial MMW RF technology (driven by developments in autonomous car navigation and 5-G wireless communications), to produce a reliable, low-SWAP-C sensor prototype addressing this requirement.

The proposed radar system will use a linear antenna array and the forward-looking synthetic aperture radar (FLSAR) concept to achieve the stated goals. A linear antenna array mounted on the rotorcraft's front end will provide the required cross-range resolution, while the transmitted signal bandwidth (up to 1 GHz) will provide downrange resolution. To achieve resolution in the vertical dimension, the radar will exploit small elevation angle deviations in the helicopter flight path, which naturally occur when the pilot prepares for landing. Overall, our radar sensor concept represents a significant shift in implementation from a hardware-heavy solution to an emphasis on signal processing and computational power, with large potential cost savings and performance improvements.

In this report we perform a detailed analysis of the 3-D imaging performance of the proposed radar system by investigating the point spread function (PSF). The emphasis here is on synthetic aperture radar (SAR) and antenna array processing, which are key to this sensor's implementation. The FLSAR concept has been recently explored by other authors. Two good examples are the Synchronous Impulse Reconstruction (SIRE)<sup>5</sup> and the Spectrally Agile Frequency-Incrementing Reconfigurable (SAFIRE)<sup>6</sup> radar systems developed at ARL between 2006 and 2016 for road clearance operations. These systems operate with ultra-wideband (UWB) waveforms in the 500- to 3000-MHz frequency range. Other research groups have developed similar radar sensors,<sup>7-9</sup> most which also operate at low frequencies. A more recent paper<sup>10</sup> proposed an MMW FLSAR system for helicopter landing very similar to the sensor described in this report, although to our knowledge that idea has remained in the concept stage.

The report is organized as follows. In Section 2 we present a high-level description of the system, in particular the sensing geometry and the relevant radar parameters. In the same section, we establish the mathematical formulation of the imaging algorithm as well as expressions for the PSF calculation. In Section 3 we discuss the three most important characteristics of the PSF: resolution, sidelobes, and grating lobes. We emphasize the importance of considering the entire 3-D space to properly quantify these metrics, which is a departure from previous analyses of 2-D imaging systems. Section 4 presents several possibilities for implementing and operating the linear antenna array and discusses the pros and cons of each solution. In Section 5 we analyze the effects of positioning errors on the radar image performance and illustrate these effects with numerical examples. Section 6 presents a simple system design case study that considers the radar waveforms, timing, and power requirements and discusses the possibility of implementing them in a practical system. We finalize with conclusions in Section 7.

## **2. Problem Formulation and Methodology**

---

The helicopter landing SAR system proposed by ARL works in a forward-looking configuration, with the goal of obtaining a 3-D image of the space around the designated landing area. The radar sensor involves a linear antenna array attached as a "front bumper" to the helicopter's fuselage. This array provides image resolution in the azimuth direction. The platform's forward motion affords diversity in the sensor's elevation angle with respect to the image area, which in turn provides image resolution in height (Fig. 1). The combination of 1-D array and platform forward motion effectively creates a 2-D synthetic array of spatial samples, subtending the same angular space as a 2-D scanning antenna array. The radar waveform's bandwidth provides resolution in the third dimension. The main

difference between the FLSAR and a conventional scanning radar equipped with a 2-D antenna array is that the physical beamforming characteristic to the latter system is replaced by the SAR image processing that takes place in the former (we call that “computational beamforming”). By this departure from existing radar system designs we seek to supplant the hardware complexity of 2-D phased arrays with the computational complexity of the FLSAR image formation process.

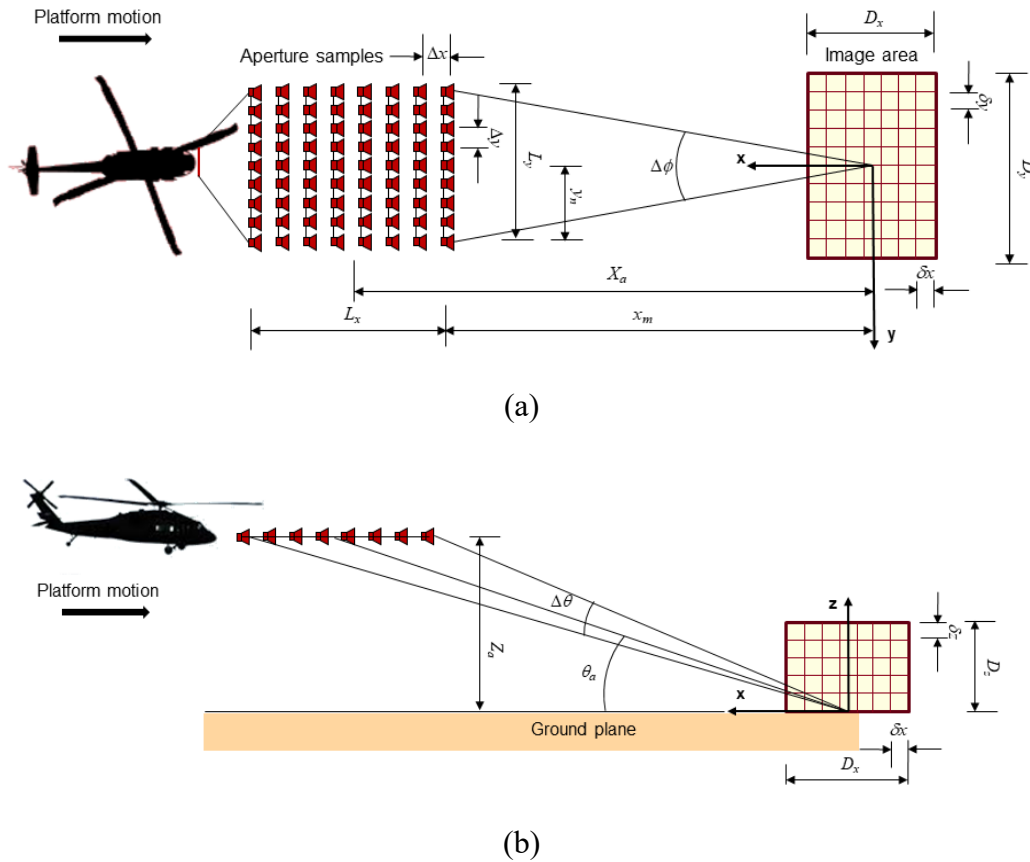


**Fig. 1** Schematic representation of the helicopter-borne radar system operating as FLSAR, showing the relevant sensing geometry from a) top view and b) side view. The small antenna diagrams mark the aperture sample positions. (Drawing not to scale.)

In this report we perform a detailed analysis of the performance achievable by the FLSAR imaging system as well as the engineering tradeoffs relevant to this problem. To this purpose, we investigate the system’s PSF, which is the image obtained by radar sensing of a point target. As is well known in the theory of imaging systems, the PSF can be interpreted as their impulse response, and its analysis is crucial in establishing performance metrics such as resolution and quantifying image artifacts such as sidelobes and grating lobes.

The SAR image formation algorithm used in this report is based on a 3-D matched filter<sup>11,12</sup> and can be described by the following equation:

$$I(x, y, z) = \frac{1}{LMN} \sum_{l=1}^L \sum_{m=1}^M \sum_{n=1}^N P_{mn}(f_l) \exp\left(j \frac{2\pi f_l}{c} (R_{mn}^t(x, y, z) + R_{mn}^r(x, y, z))\right), \quad (1)$$

where  $I(x, y, z)$  is the complex image voxel value at coordinates  $(x, y, z)$ ;  $P_{mn}(f_l)$  is the complex radar sample received at aperture indexes  $(m, n)$ ; frequency  $f_l$ ,  $R_{mn}^t(x, y, z)$  is the distance between the voxel at  $(x, y, z)$  and the transmitter aperture point  $(x_m^t, y_n^t, Z_a)$ ;  $R_{mn}^r(x, y, z)$  is the distance between the voxel at  $(x, y, z)$  and the receiver aperture point  $(x_m^r, y_n^r, Z_a)$ , and  $L, M$ , and  $N$  represent the number of samples in frequency, forward aperture direction, and lateral aperture direction, respectively (see Fig. 1 for reference). Note that this equation is valid for general bistatic radar geometries. For monostatic radar, the ranges to the transmitter and receiver are equal, and we use the equation

$$I(x, y, z) = \frac{1}{LMN} \sum_{l=1}^L \sum_{m=1}^M \sum_{n=1}^N P_{mn}(f_l) \exp\left(j \frac{4\pi f_l}{c} R_{mn}(x, y, z)\right). \quad (2)$$

The range expression is simply

$$R_{mn}(x, y, z) = \sqrt{(x_m - x)^2 + (y_n - y)^2 + (Z_a - z)^2}. \quad (3)$$

As shown elsewhere,<sup>13</sup> this imaging formula is equivalent to the popular back-projection algorithm,<sup>14</sup> with the processing taking place in the frequency domain. Although not necessarily efficient from a computational standpoint, the matched filter approach to SAR image formation is a very general and accurate procedure that can be applied to arbitrary 3-D aperture geometries and bistatic radar configurations, and it avoids many of the approximations inherent to other SAR imaging methods employed in practical systems. This approach is entirely adequate for the purpose of this investigation, where establishing theoretical performance limits is more important than various aspects of practical implementation.

To compute the PSF, we also need to find an expression for the radar signal received from a point target placed at coordinates  $(x_0, y_0, z_0)$ . This is given by the two-way Green's function describing the propagation from the transmitter to the target and back to the receiver. As customary in this type of radar propagation analysis, we neglect the magnitude variations of the point target response (PTR) across the aperture samples and retain only the phase of this response. Then, the PTR for a general bistatic geometry is given by

$$\text{PTR}_{mn}(f_l) = \exp\left(-j \frac{2\pi f_l}{c} (R_{mn}^t(x_0, y_0, z_0) + R_{mn}^r(x_0, y_0, z_0))\right). \quad (4)$$

Replacing  $P_{mn}(f_l)$  by  $\text{PTR}_{mn}(f_l)$  in Eq. 1, we obtain the following general expression for the PSF:

$$\text{PSF}(x, y, z, x_0, y_0, z_0) = \frac{1}{LMN} \sum_{l=1}^L \sum_{m=1}^M \sum_{n=1}^N \exp \left( j \frac{2\pi f_l}{c} \left( R_{mn}^t(x, y, z) + R_{mn}^r(x, y, z) - R_{mn}^t(x_0, y_0, z_0) - R_{mn}^r(x_0, y_0, z_0) \right) \right). \quad (5)$$

In the monostatic case, the PSF can be written as

$$\text{PSF}(x, y, z, x_0, y_0, z_0) = \frac{1}{LMN} \sum_{l=1}^L \sum_{m=1}^M \sum_{n=1}^N \exp \left( j \frac{4\pi f_l}{c} (R_{mn}(x, y, z) - R_{mn}(x_0, y_0, z_0)) \right). \quad (6)$$

Often the SAR imaging algorithms employ data windowing for the purpose of sidelobe reduction. If we introduce a window  $W(f_l, x_m, y_n)$  extending in the three data dimensions (frequency and two aperture directions), the PSF takes the form

$$\text{PSF}(x, y, z, x_0, y_0, z_0) = \frac{1}{LMN} \sum_{l=1}^L \sum_{m=1}^M \sum_{n=1}^N W(f_l, x_m, y_n) \exp \left( j \frac{4\pi f_l}{c} (R_{mn}(x, y, z) - R_{mn}(x_0, y_0, z_0)) \right). \quad (7)$$

At this point we need to discuss whether our imaging system operates in the near- or far-field region. As shown elsewhere,<sup>13</sup> satisfying the far-field conditions leads to simplifications of the image formation algorithm. However, to apply this simplified formulation without introducing significant phase errors, two conditions need to be met: 1) the image volume must be in the far-field region of the radar antenna (in our case, the 2-D synthetic aperture) and 2) the radar must be in the far-field region of the image volume.

For the first condition, we require  $R \geq \frac{2L_y^2}{\lambda}$ ,<sup>15</sup> where  $L_y$  is the fixed antenna array length and  $\lambda$  is the radar signal wavelength. If  $L_y = 2$  m and  $\lambda = 1$  cm, a simple numeric calculation yields a minimum range of 800 m, which is probably larger than our average radar range but of the same order of magnitude. For the second condition, we require  $R \geq \frac{2D_y^2}{\lambda}$ , where  $D_y$  is the maximum cross-range image dimension. A numeric evaluation, where we take  $D_y = 50$  m and  $\lambda = 1$  cm produces a minimum range of 500 km—this is clearly much farther than the operational range of our system (which is definitely limited to under 1 km). Consequently, our radar sensing geometry does not satisfy the far-field condition.

In the following section, we discuss the analytic calculation of the PSF and derive certain image performance metrics from that result. However, the analytic expressions developed in Section 3.1 rely on the first far-field condition previously

discussed holding true. While this condition may not be rigorously met in our practical scenario, the resolution formulas obtained there are still useful for system performance characterization and are consistent with the expressions widely used in the SAR imaging literature.

Besides the analytic calculations of the PSF, we perform extensive numeric evaluations of the same, starting directly from Eq. 7. The imaging results are illustrated with numerous 3-D graphic representations, pointing out some important departures from the conventional far-field image analysis. All the numeric simulations in this study, including the graphics, are implemented in the MATLAB software.

### 3. Image Resolution, Sidelobes, and Grating Lobes

---

#### 3.1 Analytic Expression of the PSF and Resolution

---

We start the PSF analysis by developing a closed-form expression for the triple sum in Eq. 6, from which the imaging system resolution can be derived. In all these derivations, as well as in the numerical examples throughout Section 3, we consider a monostatic radar configuration with the transmitter (Tx) and receiver (Rx) collocated in pairs and activated sequentially, one pair at a time. Here, we are not concerned with the timing or particular sequence involved in Tx–Rx activation. It is assumed that the antenna array is stationary (fixed  $x$  coordinate) while all its element pairs are activated one by one before the array moves forward to the next aperture sample in the  $x$  direction. In effect, the small antenna diagrams in Fig. 1 are a literal illustration of the aperture samples positions in our sensing scenario.

The three radar data coordinates (the frequency and the  $x$  and  $y$  coordinates of aperture samples) vary in equal increments as follows:  $f_l = l\Delta f + f_c$ , with  $f_c$  the carrier frequency and  $l = -\frac{L}{2}, \dots, \frac{L}{2} - 1$ ;  $x_m = m\Delta x + X_a$  with  $m = -\frac{M}{2}, \dots, \frac{M}{2} - 1$ ; and  $y_n = n\Delta y$  with  $n = -\frac{N}{2}, \dots, \frac{N}{2} - 1$  (for simplicity, we assume  $L$ ,  $M$ , and  $N$  to be even numbers). We rewrite the range  $R_{mn}(x, y, z)$  as

$$R_{mn}(x, y, z) = \sqrt{(m\Delta x + X_a - x)^2 + (n\Delta y - y)^2 + (Z_a - z)^2}. \quad (8)$$

At this point we invoke the assumption that the image volume is in the far-field region of the 2-D antenna aperture. Let  $\mathbf{r} = [X_a - x \quad y \quad Z_a - z]^T$  the vector connecting the middle of the 2-D synthetic aperture and the current voxel at

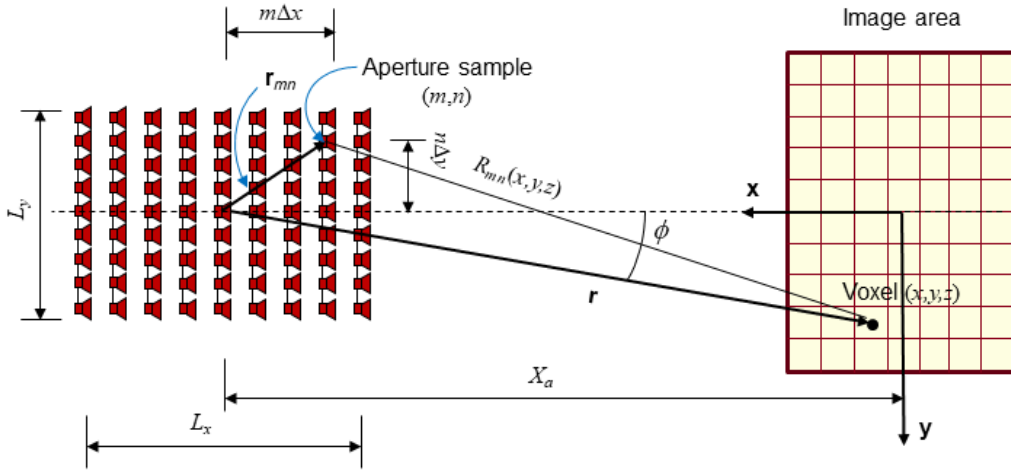
$(x, y, z)$ ; its magnitude is  $r = \sqrt{(X_a - x)^2 + y^2 + (Z_a - z)^2}$  and its direction (unit vector) is  $\hat{\mathbf{r}} = [\cos \phi \cos \theta \quad \sin \phi \cos \theta \quad \sin \theta]^T$  (see Fig. 2). As with Fig. 1, the drawings in Fig. 2 are not to scale. In fact, the image area is in practice much larger than the 2-D synthetic aperture area. Under the assumptions that  $r \gg m\Delta x$  and  $r \gg n\Delta y$ , we can expand the square root in the expression of  $R_{mn}(x, y, z)$  as a truncated Taylor series and obtain the following approximations:

$$R_{mn}(x, y, z) \cong r + m\Delta x \frac{X_a - x}{r} + n\Delta y \frac{y}{r}. \quad (9)$$

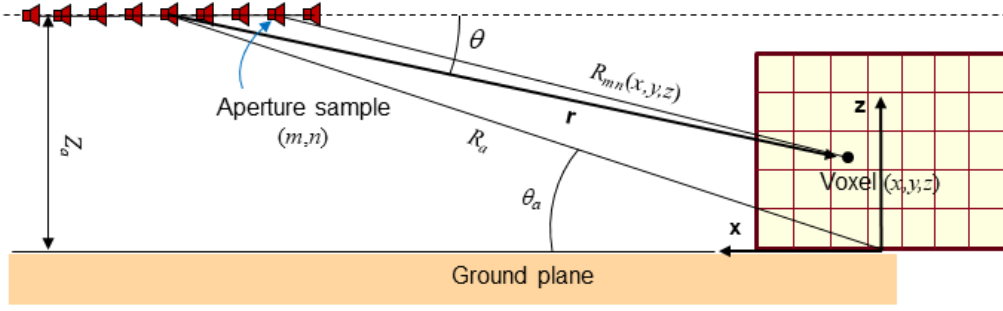
$$R_{mn}(x, y, z) \cong r + m\Delta x \cos \phi \cos \theta + n\Delta y \sin \phi \cos \theta. \quad (10)$$

Similar approximate expressions can be obtained for  $R_{mn}(x_0, y_0, z_0)$ , where in Eqs. 9 and 10 we replace  $x, y, z, r, \phi$ , and  $\theta$  with  $x_0, y_0, z_0, r_0, \phi_0$ , and  $\theta_0$ , respectively. We can then write the following equation for the PSF:

$$\text{PSF} = \frac{1}{LMN} \sum_{l=-\frac{L}{2}}^{\frac{L}{2}-1} \sum_{m=-\frac{M}{2}}^{\frac{M}{2}-1} \sum_{n=-\frac{N}{2}}^{\frac{N}{2}-1} \exp \left( j \frac{4\pi(l\Delta f + f_c)}{c} \left( (r - r_0) + m\Delta x \left( \frac{X_a - x}{r} - \frac{X_a - x_0}{r_0} \right) + n\Delta y \left( \frac{y}{r} - \frac{y_0}{r_0} \right) \right) \right). \quad (11)$$



(a)



(b)

**Fig. 2** Schematic representation of the helicopter-borne radar system operating as FLSAR, showing additional geometry elements not included in Fig. 1: a) top view and b) side view. (Drawing not to scale.)

To carry out the closed-form calculation in Eq. 11, we need to separate the triple sum into three independent factors, each representing a sum over the indexes  $l$ ,  $m$ , and  $n$ , respectively. The usual procedure is to retain only the carrier frequency sample ( $l = 0$ ) in the sums over  $m$  and  $n$ . This is a very good approximation given that our radar system has a small fractional bandwidth (or  $\frac{B}{f_c}$  ratio, where  $B$  is the bandwidth). Then we obtain the following expression:

$$\text{PSF} = \frac{\exp\left(j\frac{4\pi f_c}{c}(r-r_0)\right)}{LMN} \sum_{l=-\frac{L}{2}}^{\frac{L}{2}-1} \exp\left(j\frac{4\pi l \Delta f}{c}(r-r_0)\right) \cdot \sum_{m=-\frac{M}{2}}^{\frac{M}{2}-1} \exp\left(j\frac{4\pi f_c}{c} m \Delta x \left(\frac{X_a - x}{r} - \frac{X_a - x_0}{r_0}\right)\right) \sum_{n=-\frac{N}{2}}^{\frac{N}{2}-1} \exp\left(j\frac{4\pi f_c}{c} n \Delta x \left(\frac{y}{r} - \frac{y_0}{r_0}\right)\right) \quad (12)$$

Now each separate sum can be computed based on the geometrical series sum formula:

$$\sum_{p=-\frac{P}{2}}^{\frac{P}{2}-1} \exp(jpu) = e^{j\psi} \frac{\sin\left(\frac{Pu}{2}\right)}{\sin\left(\frac{u}{2}\right)}, \quad (13)$$

where  $\psi$  is a constant phase that can be neglected in the final expression of the PSF magnitude. The sine ratio in the right-hand side of Eq. 13 is called the digital sinc (or Dirichlet) function<sup>11</sup> and appears frequently in the analysis of electronic systems involving digital signal processing. The PSF magnitude is then

$$|\text{PSF}| = \frac{1}{LMN} \left| \frac{\sin\left(\frac{2\pi B}{c}(r-r_0)\right)}{\sin\left(\frac{2\pi \Delta f}{c}(r-r_0)\right)} \frac{\sin\left(\frac{2\pi L_x}{\lambda}\left(\frac{X_a-x}{r} - \frac{X_a-x_0}{r_0}\right)\right)}{\sin\left(\frac{2\pi \Delta x}{\lambda}\left(\frac{X_a-x}{r} - \frac{X_a-x_0}{r_0}\right)\right)} \frac{\sin\left(\frac{2\pi L_y}{\lambda}\left(\frac{y-y_0}{r} - \frac{y_0}{r_0}\right)\right)}{\sin\left(\frac{2\pi \Delta y}{\lambda}\left(\frac{y-y_0}{r} - \frac{y_0}{r_0}\right)\right)} \right|. \quad (14)$$

In the last equation, we used  $B = L\Delta f$ ,  $L_x = M\Delta x$ ,  $L_y = N\Delta y$ , and  $\lambda = \frac{c}{f_c}$ .

Alternatively, this expression can be written as a function of the angles  $\phi$  and  $\theta$ :

$$|\text{PSF}| = \frac{1}{LMN} \left| \frac{\sin\left(\frac{2\pi B}{c}(r-r_0)\right)}{\sin\left(\frac{2\pi \Delta f}{c}(r-r_0)\right)} \frac{\sin\left(\frac{2\pi L_x}{\lambda}(\cos\phi \cos\theta - \cos\phi_0 \cos\theta_0)\right)}{\sin\left(\frac{2\pi \Delta x}{\lambda}(\cos\phi \cos\theta - \cos\phi_0 \cos\theta_0)\right)} \frac{\sin\left(\frac{2\pi L_y}{\lambda}(\sin\phi \cos\theta - \sin\phi_0 \cos\theta_0)\right)}{\sin\left(\frac{2\pi \Delta y}{\lambda}(\sin\phi \cos\theta - \sin\phi_0 \cos\theta_0)\right)} \right|. \quad (15)$$

Although expressed as a closed-form equation in Eq. 14 or 15, the variation of the PSF across the 3-D radar image, when the point target location  $(x_0, y_0, z_0)$  is fixed and the image voxel coordinates  $(x, y, z)$  are variable, is very complex because all of these coordinates appear in each of the digital sinc factors. Nevertheless, by making further approximations, we can analyze each of these factors separately and understand their effects on certain image performance metrics. The complete PSF variation over the three spatial dimensions is illustrated graphically in Section 3.2, where we numerically compute its magnitude starting directly from Eq. 6.

(1) The first digital sinc factor in Eq. 14 determines the PSF variation with range  $r$ .

To obtain the range resolution, we compute the main lobe's null-to-null width for this digital sinc function: this can be readily found as  $\frac{c}{B}$ . By convention,

the resolution is taken as half the main lobe's null-to-null width, or  $\delta r = \frac{c}{2B}$ .

Furthermore, we have  $r = (X_a - x)\cos\phi \cos\theta + y \sin\phi \cos\theta + (Z_a - z)\sin\theta$ . Since  $X_a - x \gg |y|$  and  $X_a - x \gg Z_a - z$ , while  $\phi$  and  $\theta$  are small angles (less than  $10^\circ$ ), we can approximate  $r \approx (X_a - x)\cos\phi \cos\theta$ . A similar approximate expression can be derived for  $r_0$ . Additionally, in the main lobe region, the

current voxel is close to the point target, so  $\phi \cong \phi_0$  and  $\theta \cong \theta_0$ . Given all these considerations, we can write

$$\frac{\sin\left(\frac{2\pi B}{c}(r-r_0)\right)}{\sin\left(\frac{2\pi\Delta f}{c}(r-r_0)\right)} \cong \frac{\sin\left(\frac{2\pi B}{c}\cos\phi_0\cos\theta_0(x-x_0)\right)}{\sin\left(\frac{2\pi\Delta f}{c}\cos\phi_0\cos\theta_0(x-x_0)\right)}. \quad (16)$$

From this result, we derive the resolution in the  $x$  direction (or downrange resolution) as  $\delta x = \frac{c}{2B\cos\phi_0\cos\theta_0}$ . This formula shows that the downrange resolution theoretically depends on the point target location via  $\phi_0$  and  $\theta_0$ . However, given that  $\phi_0$  and  $\theta_0$  are small angles,  $\cos\phi_0$  and  $\cos\theta_0$  are always very close to 1 (for instance,  $\cos 10^\circ = 0.98$ ); therefore, the resolution dependence on these angles (and consequently, the point target location) is very weak. For all practical purposes, we can use the formula  $\delta x = \frac{c}{2B}$ , with very good accuracy.

As a side note, the terms containing  $y$  and  $z$  in the  $r$  expression cannot be neglected any longer if the angles  $\phi_0$  and  $\theta_0$  become large. In that case, the first digital sinc factor of the PSF may have a significant impact on the resolutions in the  $y$  and  $z$  directions as well.

- (2) The second digital sinc factor in Eq. 14 determines the resolution in elevation. To show this, we write

$$\frac{X_a - x}{r} = \cos\phi\cos\theta = \cos\phi\sqrt{1 - \sin^2\theta} = \cos\phi\sqrt{1 - \left(\frac{Z_a - z}{r}\right)^2}. \quad (17)$$

Since  $\phi$  and  $\theta$  are always small, it is safe to assume that  $\cos\phi \cong 1$  and approximate the square root by a truncated Taylor series expansion. Then we obtain  $\frac{X_a - x}{r} \cong 1 - \frac{(Z_a - z)^2}{2r^2}$ . If we consider voxels in the main lobe region, which is the vicinity of the point target, we have

$$\frac{X_a - x}{r} - \frac{X_a - x_0}{r_0} \cong \frac{(Z_a - z)^2}{2r^2} - \frac{(Z_a - z_0)^2}{2r_0^2} \cong \frac{Z_a - z_0}{r_0^2}(z - z_0) = \frac{\sin\theta_0}{r_0}(z - z_0), \quad (18)$$

and the second digital sinc factor becomes

$$\frac{\sin\left(\frac{2\pi L_x}{\lambda}\left(\frac{X_a - x}{r} - \frac{X_a - x_0}{r_0}\right)\right)}{\sin\left(\frac{2\pi\Delta x}{\lambda}\left(\frac{X_a - x}{r} - \frac{X_a - x_0}{r_0}\right)\right)} \cong \frac{\sin\left(\frac{2\pi L_x \sin\theta_0}{\lambda r_0}(z - z_0)\right)}{\sin\left(\frac{2\pi\Delta x \sin\theta_0}{\lambda r_0}(z - z_0)\right)}. \quad (19)$$

The main lobe's null-to-null width for the function in Eq. 19 is  $\frac{\lambda r_0}{L_x \sin\theta_0}$ .

Consequently, the resolution in the  $z$  direction is  $\delta z = \frac{\lambda r_0}{2L_x \sin\theta_0}$ .

Again, we notice that this resolution depends on the point target location via  $r_0$  and  $\sin\theta_0$ . Since  $r_0$  varies in a tight range across the image volume, the resolution dependence on  $r_0$  is weak. However,  $\sin\theta_0$  can have a large variation within the image volume and depends primarily on  $z_0$ . Thus, the elevation resolution is better for larger angles  $\theta_0$  (or targets closer to the ground) than for targets placed at some height away from the ground plane. An interesting case occurs when  $z_0 = Z_a$  or  $\theta_0 = 0^\circ$ : in that case, we have no resolution in elevation. A practical consequence is that we must make sure that the aperture height  $Z_a$  is always larger than the maximum image height. In general, a larger aperture height is preferable for this FLSAR system since it offers better elevation resolution. The large sensitivity of this resolution with respect to the target location is the effect of the severe squint angle of the forward synthetic aperture with respect to the image volume.

For the remainder of this report, we take the nominal  $z$ -directed resolution of the FLSAR system as that obtained for a point target placed in the coordinate system origin,  $\delta z = \frac{\lambda R_a}{L_x \sin\theta_a}$ , where  $R_a = \sqrt{X_a^2 + Z_a^2}$ , with the implicit understanding that in fact  $\delta z$  varies across the image volume with the point target location.

- (3) The third digital sinc factor dictates the resolution in azimuth or cross-range dimension. In the main lobe region, where the current voxel is close to the point target location, we can approximate  $r \cong r_0$  and write

$$\frac{\sin\left(\frac{2\pi L_y}{\lambda}\left(\frac{y}{r} - \frac{y_0}{r_0}\right)\right)}{\sin\left(\frac{2\pi\Delta y}{\lambda}\left(\frac{y}{r} - \frac{y_0}{r_0}\right)\right)} \cong \frac{\sin\left(\frac{2\pi L_y}{\lambda r_0}(y - y_0)\right)}{\sin\left(\frac{2\pi\Delta y}{\lambda r_0}(y - y_0)\right)}. \quad (20)$$

The main lobe's null-to-null width of this digital sinc function is  $\frac{\lambda r_0}{L_y}$  and the resolution in the  $y$  direction is  $\delta y = \frac{\lambda r_0}{2L_y}$ .

Although we again notice a variation of the resolution with the point target location (via  $r_0$ ), as already established, this variation is weak and we can approximate  $r_0 \cong R_a$ . In that case, the cross-range resolution becomes

$$\delta y = \frac{\lambda R_a}{2L_y} \text{ uniformly across the image volume.}$$

Note that the previous analysis of the image resolution in the three Cartesian directions is only valid for small angles  $\phi$  and  $\theta$ . More-exact expressions for the main lobe widths of the digital sinc factors involved in the PSF of the FLSAR system were derived by Liao et al.,<sup>16</sup> without relying on the small angle assumptions. However, it can be shown that, for the FLSAR system under consideration in this study, where  $\phi$  and  $\theta$  are small (below  $10^\circ$ ), those expressions reduce to the simple resolution formulas obtained in this section.

Other important information on the 3-D radar image conveyed by the PSF analysis is the location of the grating lobes. These are secondary peaks of the PSF with spatial locations given by the nulls of the sine functions in the three denominators in Eq. 14. For brevity, here we only show the calculations relevant to the cross-range grating lobe location; the derivations for the other two dimensions are similar, and only the final results are listed.

As discussed in Section 3.3, the grating lobes generated by the second and third digital sinc factors of the PSF always occur along circles centered in the middle of the 2-D synthetic aperture and passing through the point target location, which means that  $r = r_0$  at the grating lobe locations. Then the denominator of the third digital sinc function is  $\sin\left(\frac{2\pi\Delta y}{\lambda r_0}(y - y_0)\right)$  along these circles. Its nulls occur when

the sine argument equals  $p\pi$  (where  $p$  is an integer), or  $y = y_0 + p\frac{\lambda r_0}{2\Delta y}$ .

Consequently, the distance between two consecutive grating lobes (also known as the unambiguous cross-range swath) is  $\frac{\lambda r_0}{2\Delta y}$ . By considering  $r_0 \cong R_a$ , we obtain

the nominal unambiguous cross-range swath  $D_y = \frac{\lambda R_a}{2\Delta y}$ .

For the elevation direction, a similar analysis of the second digital sinc factor yields the unambiguous swath  $D_z = \frac{\lambda r_0}{2\Delta x \sin \theta_0}$ . As with the elevation resolution, this

image metric depends on the point target location. The last formula suggests that the unambiguous elevation swath becomes larger as the point target is moved higher, away from the ground plane. We take the nominal value for this metric as  $D_z = \frac{\lambda R_a}{2\Delta x \sin \theta_a}$ , which is obtained for a point target placed in the coordinate system origin.

The unambiguous downrange swath is obtained from the nulls of the first digital sinc denominator, and its value is  $D_x = \frac{c}{2\Delta f}$ . Note that the grating lobes generated

by this factor are not located along the circles mentioned previously but along the line connecting the middle of the 2-D synthetic aperture and the point target. Further analysis of the 3-D spatial distribution and magnitude of the grating lobes is performed in Sections 3.3 and 3.5 of this report.

### 3.2 Numeric Examples of PSF

---

In this section we present some numerical examples of PSF for the FLSAR configuration described in Section 2. We pick a set of representative values for the SAR parameters illustrated in Fig. 1:

- Carrier frequency  $f_c = 35$  GHz (Ka-band)
- Bandwidth  $B = 500$  MHz, from 34.7 to 35.2 GHz
- Fixed aperture width  $L_y = 2$  m
- Synthetic aperture length  $L_x = 15$  m
- Radar platform height  $Z_a = 26$  m
- Average horizontal range  $X_a = 150$  m; horizontal range varies from 157.5 to 142.5 m
- Number of samples in frequency  $L = 101$ , spaced 5 MHz apart
- Number of samples in azimuth  $N = 51$ , spaced 4 cm apart (in  $y$  direction)
- Number of samples in elevation  $M = 51$ , spaced 0.3 m apart (in  $x$  direction)

The angular parameters can be derived as follows:

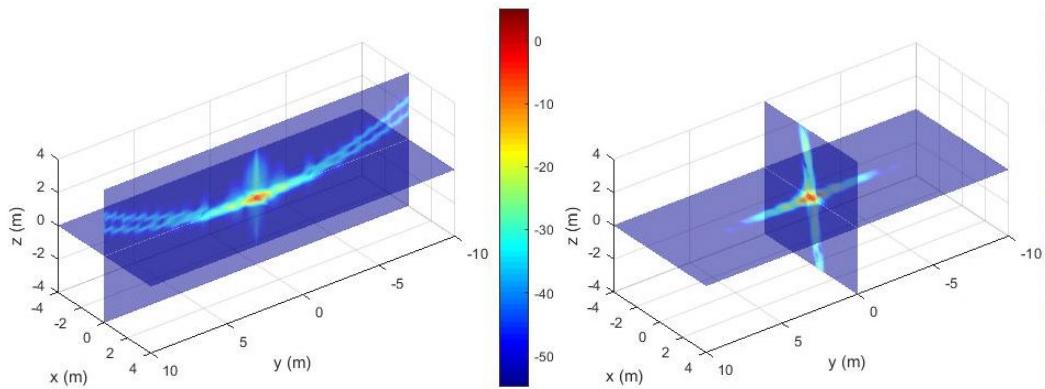
- Azimuth integration angle:  $\Delta\phi = 0.8^\circ$

- Elevation integration angle:  $\Delta\theta = 1^\circ$
- Slant angle:  $\theta_a = 10^\circ$  (varying from  $9.4^\circ$  to  $10.4^\circ$  across the aperture)
- Azimuth sampling step:  $0.016^\circ$
- Elevation sampling step:  $0.02^\circ$

By applying the equations established in Section 3.1, we obtain the following nominal resolutions in the three Cartesian directions:  $\delta x = 0.3$  m,  $\delta y = 0.3$  m, and  $\delta z = 0.25$  m. As discussed in that section, the resolution in the  $z$  direction is variable: it ranges from 0.25 m (when  $z_0 = 0$ ) to 0.5 m (when  $z_0 = 12.5$  m). In terms of unambiguous ranges (or, more exactly, distance between successive grating lobes), we have  $D_x = 30$  m,  $D_y = 16$  m, and  $D_z = 12.5$  m (the last number is obtained for  $z_0 = 0$ ).

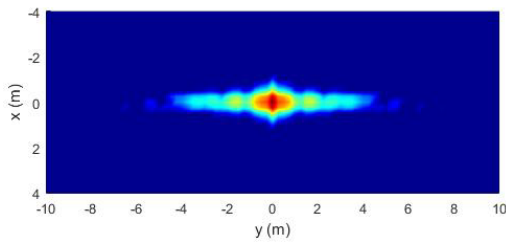
The 3-D image representing the PSF with the point target placed in the origin is shown in Figure 3. Note that we tried to represent the image from as many points of view as possible to give the reader a complete picture of the features under investigation. Thus, Figs. 3a and 3b are planar cuts through the 3-D image in a perspective view, whereas Figs. 3c through 3e are representations of the image in the principal Cartesian planes,  $x$ - $y$ ,  $y$ - $z$ , and  $x$ - $z$ , respectively. Furthermore, Figs. 3f, 3g, and 3h are axial cuts through the 3-D image along the  $x$ ,  $y$ , and  $z$  axes, respectively.

In obtaining the images in Fig. 3, we only applied a tapered window in the frequency dimension of the radar data. Specifically, a Hanning window was used in the frequency domain. However, we did not window the data in any of the two aperture dimensions. This allowed us to get a clear representation of the sidelobes arising from the sensing geometry and SAR image formation algorithm. Consequently, the main lobe width of the PSF matches the analytic expressions in the  $y$  and  $z$  directions but is about twice as wide as the theoretical prediction in the  $x$  direction due to the frequency domain window. At the same time, we see significant sidelobe levels in the  $y$  and  $z$  directions (Figs. 3g and 3h), while the  $x$ -directed sidelobes are strongly suppressed (Fig. 3f). An additional detail about the graphics in Fig. 3 is that the pseudo-color plots represent image magnitude with a dynamic range of 60 dB, while the line plots represent the same magnitude with 80 dB of dynamic range. In all images, the peak value is 5 dB.

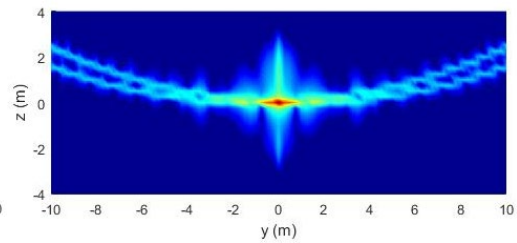


(a)  
(b)

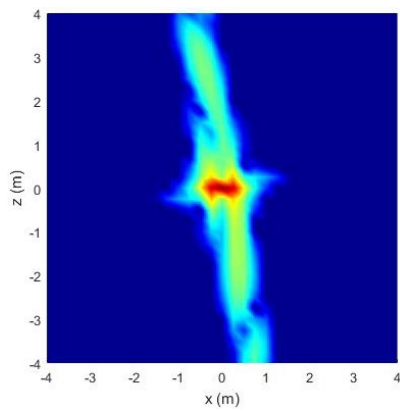
(b)  
(a)



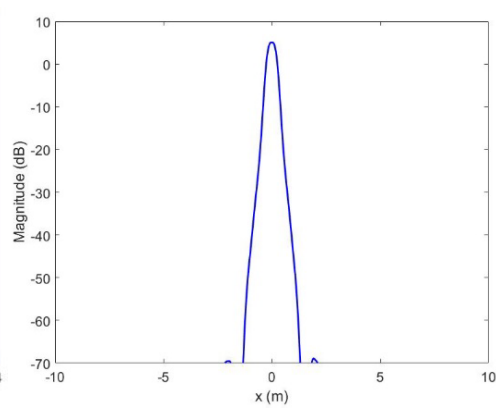
(c)



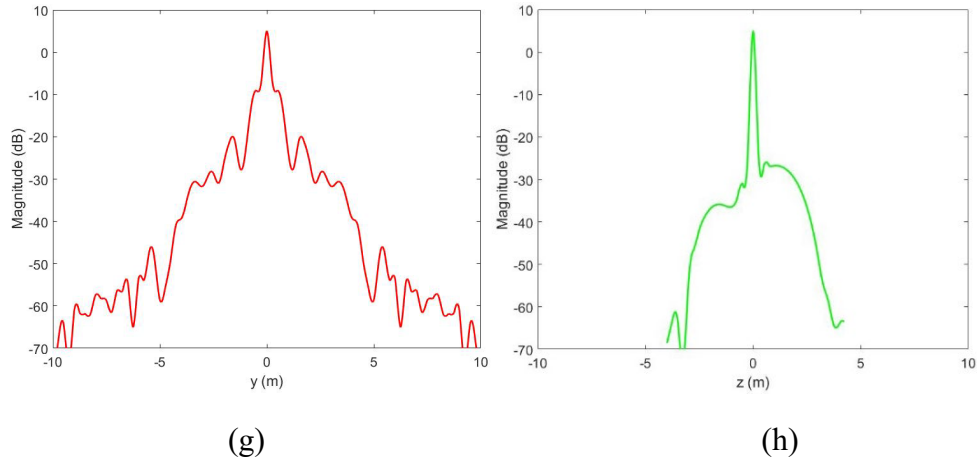
(d)



(e)

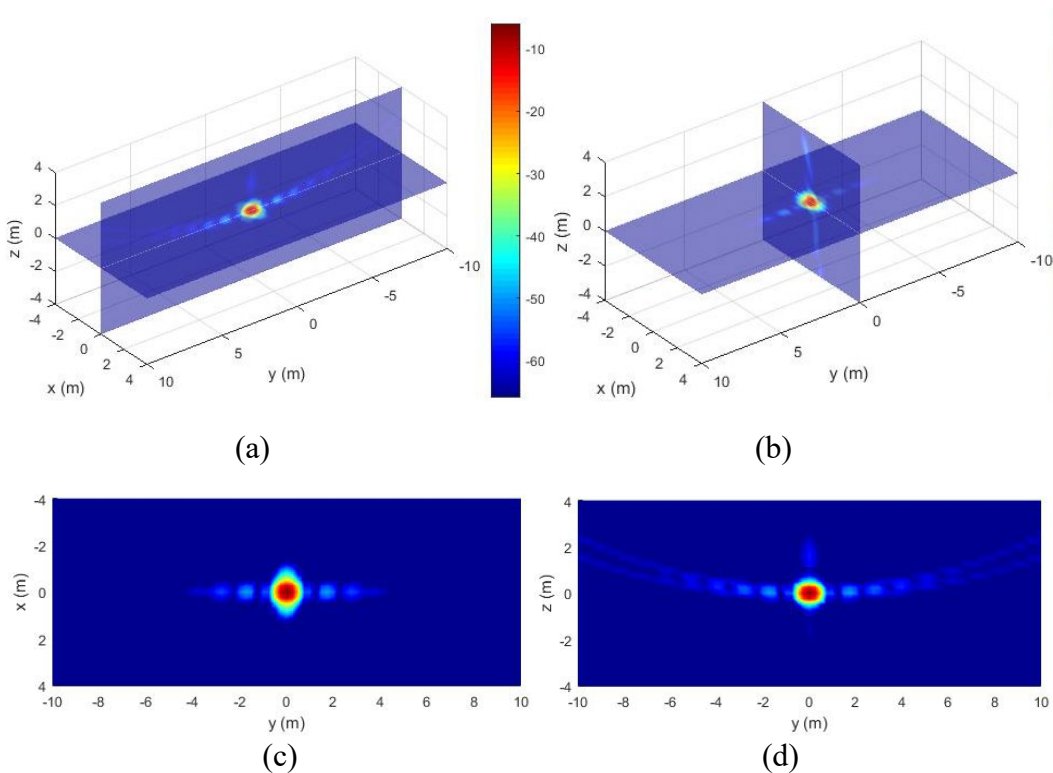


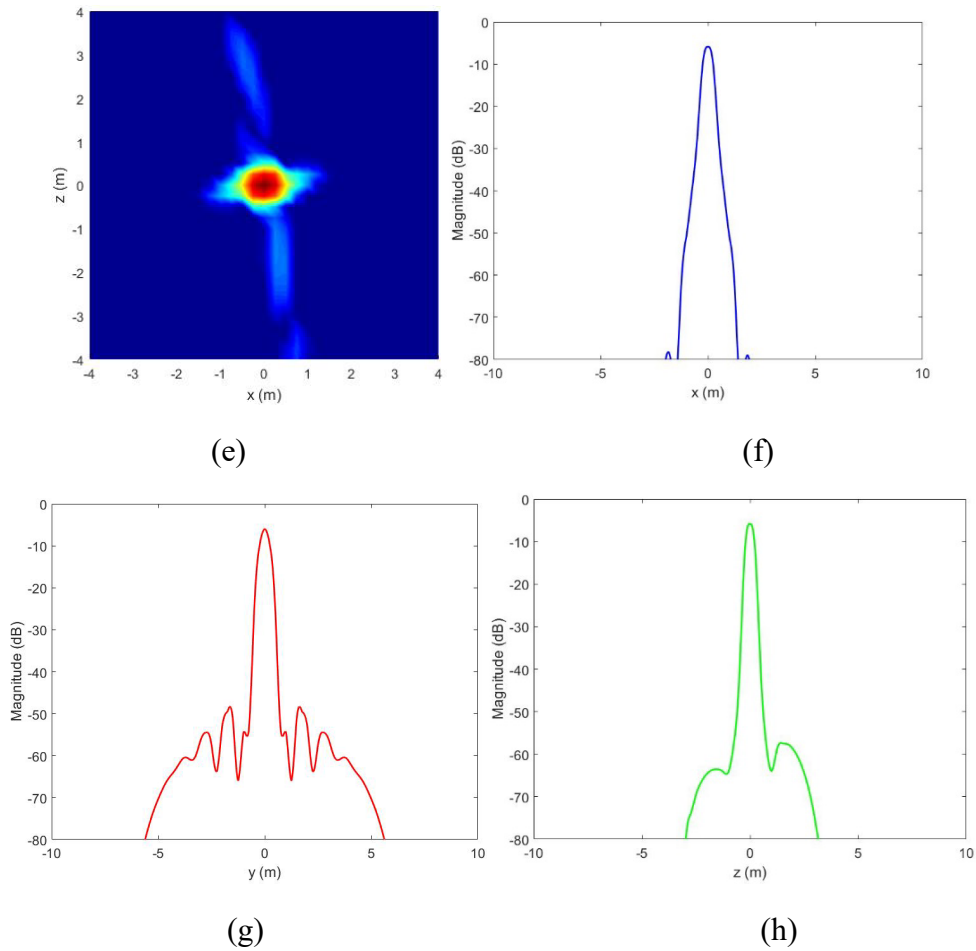
(f)



**Fig. 3** Graphic representation of the PSF for the radar system parameters considered in this section, with the point target placed in the origin of the coordinate system: a) x-y and y-z planes, perspective view; b) x-y and x-z planes, perspective view; c) x-y plane; d) y-z plane; e) x-z plane; f) cut along the x axis; g) cut along the y axis; and h) cut along the z axis. A Hanning window is applied to the radar data in the frequency dimension only. The color bar for the pseudo-color plots represents magnitude in decibels.

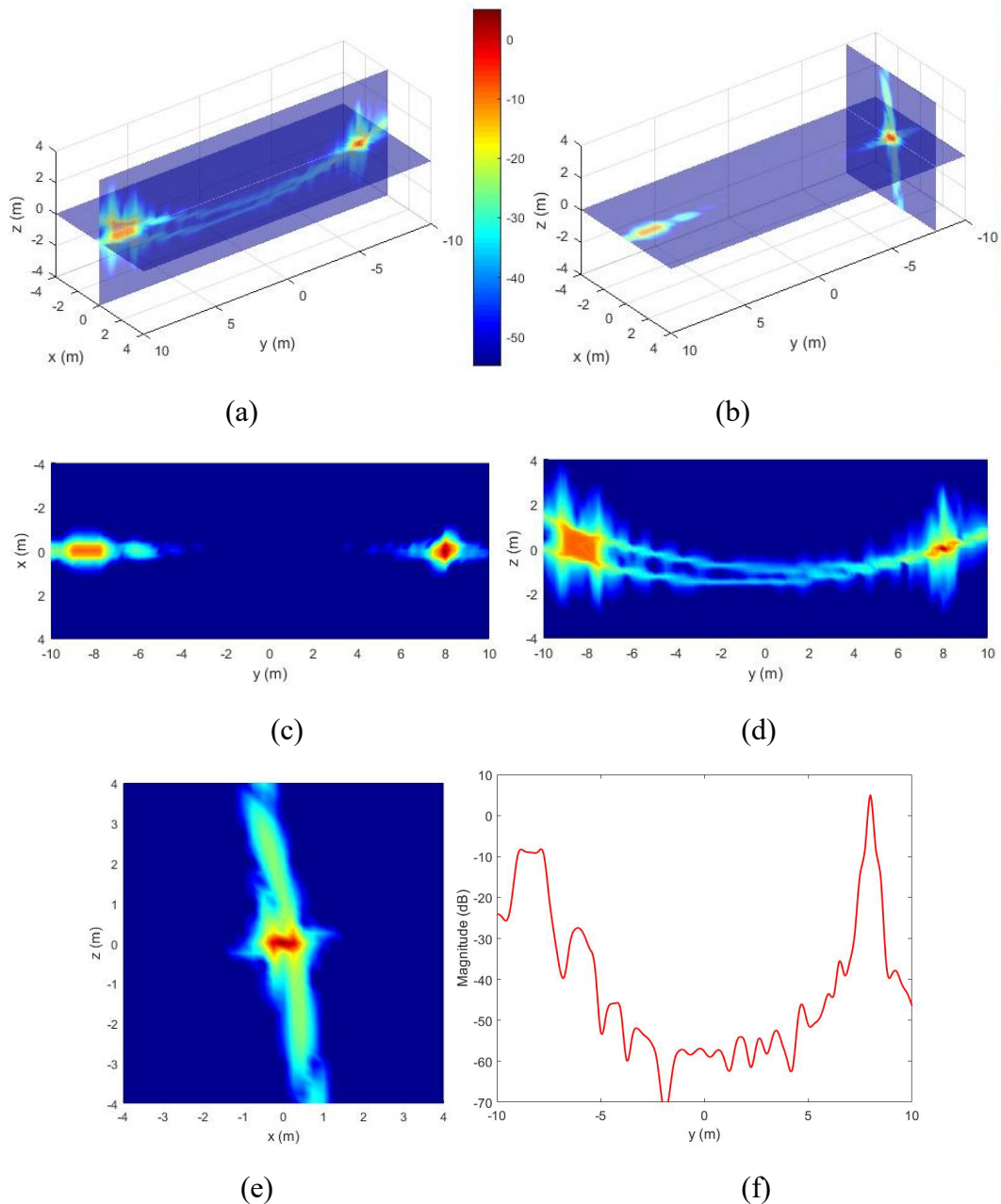
Figure 4 represents the PSF obtained for the same radar parameters after applying Hanning windows in all three dimensions of the radar data. As expected, the resolution numbers degrade in all dimensions (approximately 0.6 m, 0.6 m, and 0.5 m in the three Cartesian directions, respectively), but, at the same time, the sidelobes are suppressed to at least 50 dB below the peak.





**Fig. 4** Graphic representation of the PSF for the radar system parameters considered in this section, with the point target placed in the origin of the coordinate system: a) x-y and y-z planes, perspective view; b) x-y and x-z planes, perspective view; c) x-y plane; d) y-z plane; e) x-z plane; f) cut along the x axis; g) cut along the y axis; and h) cut along the z axis. For this numerical example, the radar data was tapered in all three dimensions using Hanning windows.

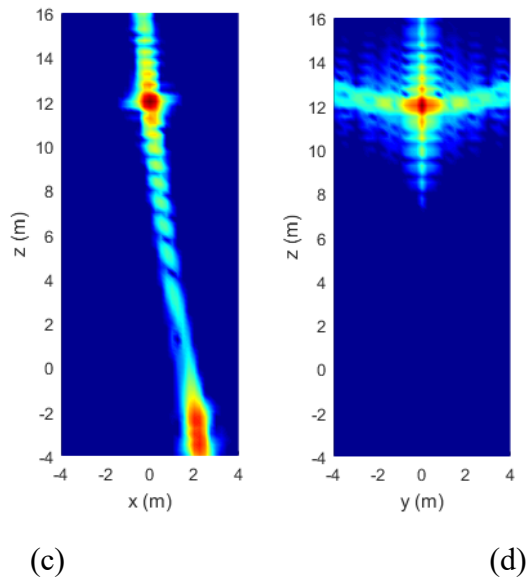
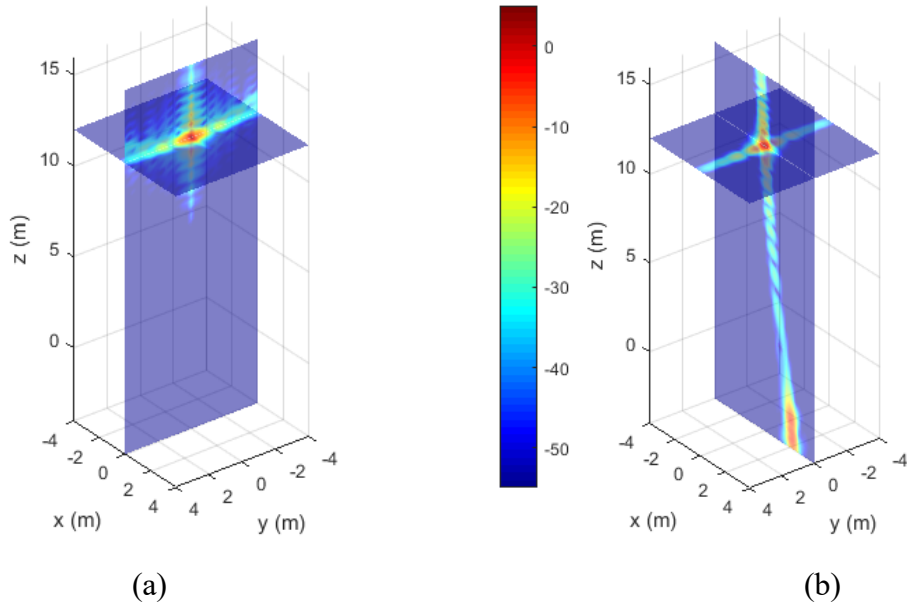
In the next numerical example, we move the point target to coordinates  $x_0 = 0$ ,  $y_0 = 8$  m, and  $z_0 = 0$  and plot the radar image in Fig. 5. (Note: In the numerical example in Fig. 5, as well as the remainder of this report, we use the same data windowing scheme as in the original example from Fig. 3.) The interesting new feature present in this image is the grating lobe showing up around the coordinates  $x = 0$ ,  $y = -8$  m, and  $z = 0$ , as previously predicted (as a reminder, the predicted distance between grating lobes in the y direction is  $D_y = 16$  m).



**Fig. 5** Graphic representation of the PSF for the radar system parameters considered in this section, with the point target placed at  $x_0 = 0$ ,  $y_0 = 8$  m, and  $z_0 = 0$ : a) x-y and y-z planes, perspective view; b) x-y and y = 8 m planes, perspective view; c) x-y plane; d) y-z plane; e) y = 8 m plane; and f) cut along the y axis

In the final numerical example of this section, the point target is placed at coordinates  $x_0 = 0$ ,  $y_0 = 0$ , and  $z_0 = 12$  m, with the radar image shown in Fig. 6. This configuration illustrates the fact that the elevation resolution depends on the point target's height  $z_0$ . Thus, the PSF's main lobe along the  $z$  axis has a half-width of about 0.5 m compared with 0.25 m for a point target placed in the origin (compare

Figs. 3h and 6f). Another notable image feature is the grating lobe in the elevation direction, which is visible around  $z = -3$  m.



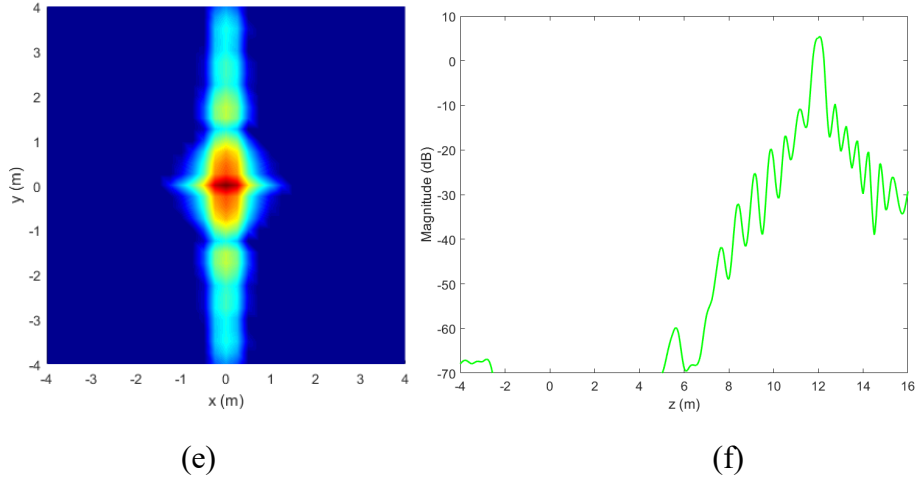


**Fig. 6** Graphic representation of the PSF for the radar system parameters considered in this section, with the point target placed at  $x_0 = 0$ ,  $y_0 = 0$ , and  $z_0 = 12$  m: a)  $z = 12$  m and  $y$ - $z$  planes, perspective view; b)  $z = 12$  m and  $x$ - $z$  planes, perspective view; c)  $x$ - $z$  plane; d)  $y$ - $z$  plane; e)  $z = 12$  m plane; and f) cut along the  $z$  axis

### 3.3 Sidelobe and Grating Lobe Analysis

As mentioned in Section 2 and illustrated in Section 3.2, the far-field assumptions on which SAR imaging system analysis is often based are not valid for our sensing geometry. One striking departure from the far-field model visible in the numerical examples of the previous section is the orientation of the sidelobes and grating lobes. Thus instead of showing up along straight lines (as predicted for the far-field case), the sidelobes and grating lobes describe curved trajectories in the 3-D space as an effect of the near-field imaging geometry. Another important conclusion from the graphs in Section 3.2 is that the sidelobes and grating lobes do not align with the Cartesian axes; therefore, simply plotting image cuts along the  $x$ ,  $y$ , or  $z$  axes (as in Figs. 3f through 3h, for instance) does not provide a good representation of these image artifacts by underestimating their magnitudes.

In this section, we perform a detailed analysis of the sidelobe line geometry and point to the correct way of evaluating their magnitudes. For this purpose we need to consider the sidelobe distribution throughout the entire 3-D space. Note that this analysis is much more complex than what is typically encountered in 2-D imaging geometries, which is treated in the vast majority of the SAR-related literature. In the interest of conciseness, we do not provide rigorous mathematical proofs to some of the statements and formulas presented in this section; however, the numerical examples shown here clearly support these statements. A separate work dedicated solely to the mathematical proofs of certain equations relevant to SAR image analysis is planned.

The first important observation about the PSF sidelobes produced by the FLSAR geometry described in Fig. 1 is that they are distributed on the surfaces of four spheres: each sphere is centered at one of the four corners of the 2-D aperture and passes through the location of the point target. In the following, we call these spheres “sidelobe surfaces”. Note that for the imaging geometry of this radar system, characterized by small integration angles (on the order of  $1^\circ$ ), the surfaces of the four spheres are extremely close to one another around the point target region and therefore almost indistinguishable. Consequently, to get a good representation of the sidelobe lines in this region, it suffices to consider the surface of just one sphere, with the center  $(x_c, y_c, z_c)$  placed in the middle of the 2-D aperture (specifically,  $x_c = X_a = 150$  m,  $y_c = 0$ , and  $z_c = Z_a = 26$  m) and passing through the origin (the location of the point target). The analytic equation of such sphere is

$$x^2 - 2xx_c + y^2 - 2yy_c + z^2 - 2zz_c = 0. \quad (21)$$

Figure 7 shows the 3-D SAR image “painted” on the surface of this sphere (to be precise, a limited sector of it), obtained for the radar parameters in Section 3.2. Note that this is exactly the same 3-D SAR image represented in Fig. 3 but at different sample points in the 3-D space, which emphasize the lines of prominent sidelobes and grating lobes. Note the overall image peak at the target location (the coordinate system origin).

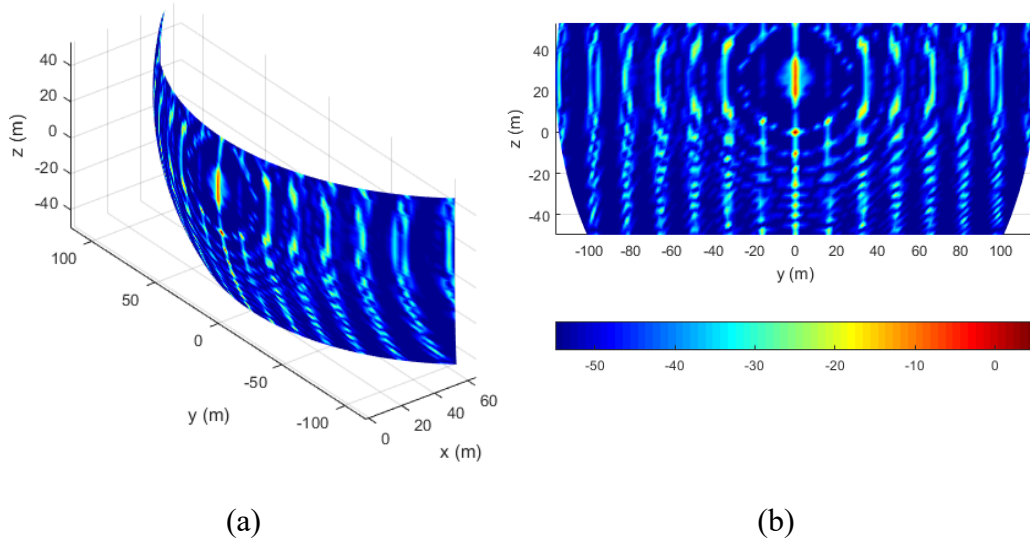


**Fig. 7** 3-D representation of the PSF obtained with the FLSAR system “painted” on the surface of the sphere described by Eq. 21: a) perspective view and b) view along the x axis

The next observation is that the PSF sidelobes tend to be distributed along curves of constant  $y$  (these are the vertical lines in Fig. 7b) as well as curves of constant  $x$  (circles in Fig. 7b). To be more precise, the sidelobe lines are obtained at the

intersection of the sidelobe surface (described by Eq. 21) and the planes described by the equations  $y = \text{constant}$  and  $x = \text{constant}$ , respectively. In 3-D representation, both these sets of curves are circles in vertical planes. The prominent image points obtained at the intersections of these sets of curves are the grating lobes. Note that the grating lobes are located at regular intervals  $D_y = 16$  m in the  $y$  direction and at regular intervals in the  $x$  direction (but not in the  $z$  direction, as shown later).

As a general trend, the sidelobes and grating lobes nearest to the target location are the strongest; their magnitudes decrease for more-distant voxels (these are what we call the “higher order” sidelobes and grating lobes). Therefore, we are primarily concerned with the region close to the target location, where these image artifacts are most prominent. A close-up representation of the PSF around the origin, “painted” on the sidelobe surface/sphere, is shown in Fig. 8.

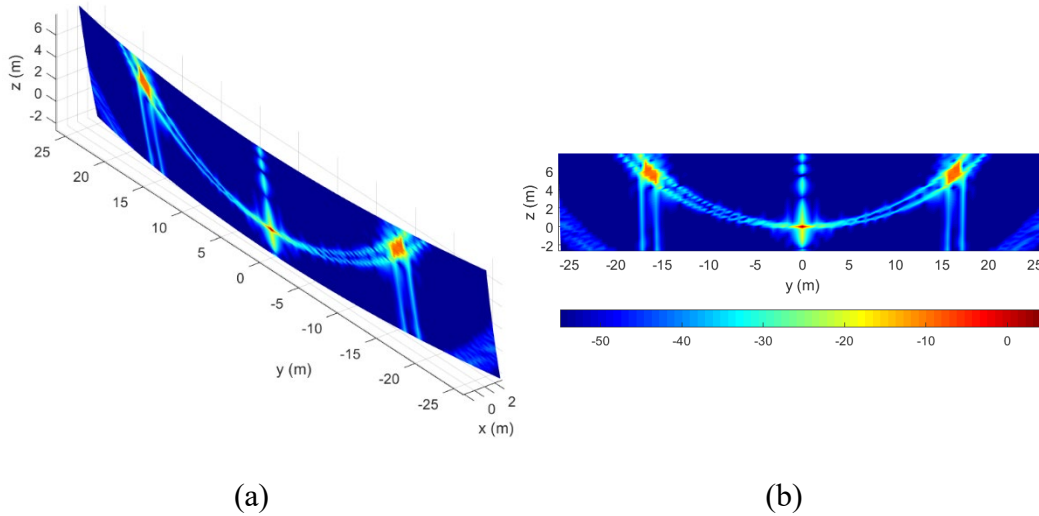


**Fig. 8** Close-up 3-D representation of the PSF obtained with the FLSAR system “painted” on the surface of the sphere described by Eq. 21: a) perspective view and b) view along the  $x$  axis

The image in Fig. 8 is reminiscent of the  $y$ - $z$  plane representation shown in Fig. 3d, although the two surfaces are not identical (note that the sphere surface is slightly tilted with respect to the  $y$ - $z$  plane). However, the two circular arcs visible in both images, along which the sidelobes are distributed, are identical between Figs. 8 and 3b. The fact that we obtain two distinct circles as sidelobe curves is due to the existence of two separate sidelobe surface spheres, each centered at one end of the antenna array in the  $y$  direction. An additional feature visible in Fig. 8 is the pair of grating lobes present around the coordinates  $y = \pm 16$  m. Note that these features are “stretched” between the two sidelobe circles previously mentioned.

The geometrical considerations presented so far suggest that in order to quantitatively evaluate the side- and grating lobes we need to consider image points

placed along the sidelobe curves already discussed. The equations of these curves passing through the target location (or coordinate system origin) can be obtained as follows:

- Intersection of the sphere described by Eq. 21, where  $x_c = X_a$ ,  $y_c = \pm \frac{L_y}{2}$ ,  $z_c = Z_a$ , with the  $x = 0$  plane. We obtain the equation

$$y^2 - 2yy_c + z^2 - 2zZ_a = 0, \quad (22)$$

which represents a circle in the  $y$ - $z$  plane. To calculate the coordinates of points along this circle, we let  $y$  vary as a free parameter and compute  $z$  from

$$z = Z_a - \sqrt{Z_a^2 - y^2 + 2yy_c}. \quad (23)$$

- Intersection of the sphere described by Eq. 21, where  $x_c = X_a$ ,  $y_c = \pm \frac{L_y}{2}$ ,  $z_c = Z_a$ , with the  $y = 0$  plane. We obtain the equation

$$x^2 - 2xX_a + z^2 - 2zZ_a = 0, \quad (24)$$

which represents a circle in the  $x$ - $z$  plane. To calculate the coordinates of points along this circle, we let  $z$  vary as a free parameter and compute  $x$  from

$$x = X_a - \sqrt{X_a^2 - z^2 + 2zZ_a}. \quad (25)$$

The magnitudes of the image points along these curves, representing the true sidelobe levels, are shown in Fig. 9. The abscissa in these plots is the linear coordinate measured along those curves. Note that these graphs look radically different from those in Figs. 3g and 3h, which represent the image voxel magnitudes along the  $y$  and  $z$  axes, respectively (to be fair, the abscissas in the two pairs of graphs have slightly different meanings). This underscores the idea that plotting simple axial cuts along the Cartesian coordinate system axes (as in Section 3.2) is misleading with regards to sidelobe analysis.

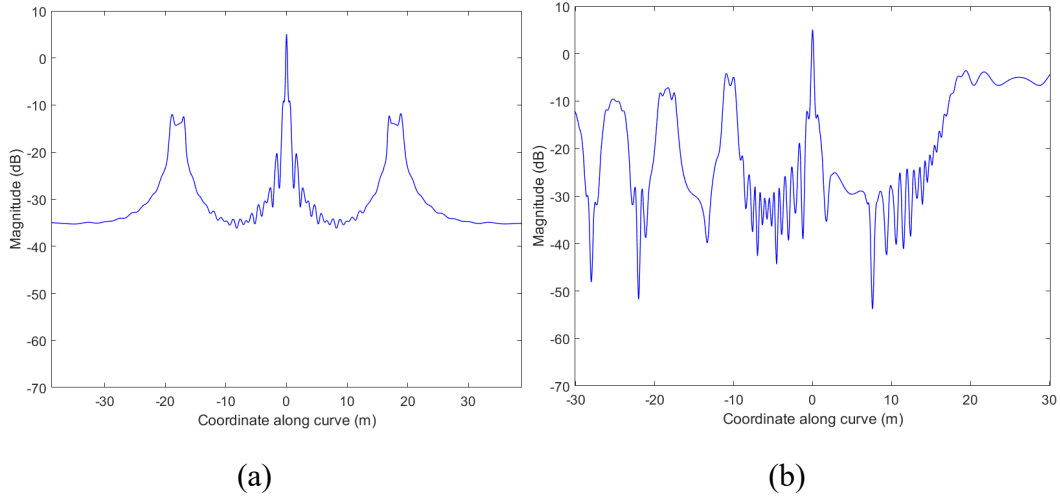


**Fig. 9** Voxel magnitude along the sidelobe lines passing through the origin (or target location), evaluated on the circles a) in the  $y$ - $z$  plane (described by Eq. 22) and b) in the  $x$ - $z$  plane (described by Eq. 24)

One shortcoming of the Fig. 9a plot is that it misses the grating lobe true peaks, visible in Fig. 8. To capture those peaks, we consider a circle obtained at the intersection of the sphere centered at  $x_c = X_a$ ,  $y_c = 0$ ,  $z_c = Z_a$ , and the  $x = 0$  plane. The difference between the three circles in the  $x = 0$  plane, obtained for  $y_c = 1$  m, 0, and  $-1$  m, respectively, is illustrated in Fig. 10a. The magnitude of the image points obtained along those circles is shown in Fig. 10b. The blue-line graph ( $y_c = 1$  m) captures primarily the sidelobes, whereas the red-line graph ( $y_c = 0$ ) captures primarily the grating lobes.

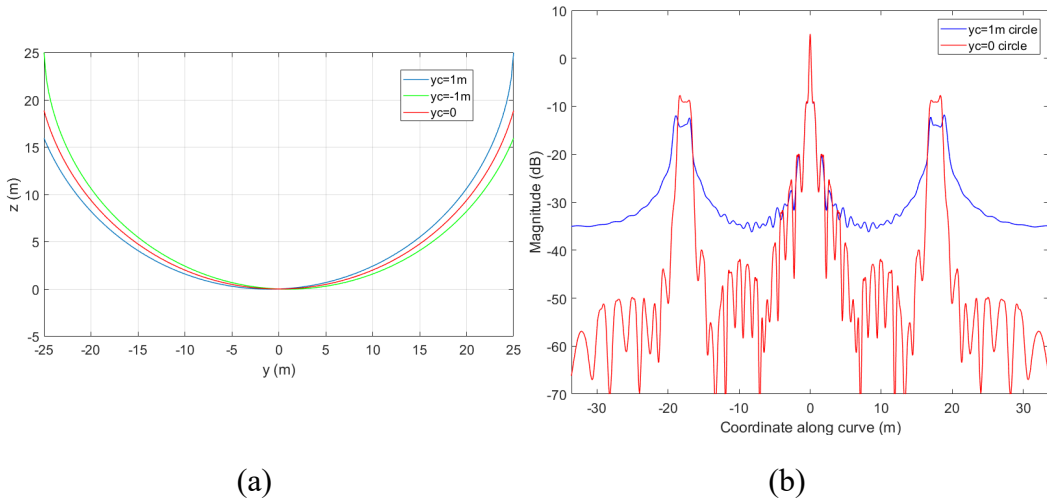


**Fig. 10** a) Sidelobe circles in the  $y$ - $z$  plane obtained for various values of  $y_c$ , and b) voxel magnitude along two of these circles, emphasizing the sidelobes (blue line) and the grating lobes (red line)

### 3.4 Imaging Performance Levers and Tradeoffs

---

This section discusses the impact of the image artifacts on the image quality and possible mitigation techniques. As already pointed out, the SAR-type processing in each of the radar data dimensions (frequency, antenna array or physical aperture, and forward synthetic aperture) has major effects on the corresponding image dimensions: downrange ( $x$ -directed), cross-range ( $y$ -directed), and elevation ( $z$ -directed), respectively. The relevant radar data processing parameters are 1) the data variation range (which dictates the resolution), 2) the sampling rate (which dictates the distance between grating lobes), and 3) the amplitude weighting (which can control the sidelobe levels).

Ideally, we would like to have large radar data variation range (for good resolution, or a narrow main lobe), small sampling steps (to push the first-order grating lobes as far as possible from the main lobe), and tapered data amplitude (to reduce the sidelobe levels). Unfortunately, simultaneously achieving all these data characteristics is very difficult due to physical, operational, and technological constraints, as well as inherent tradeoffs in radar signal processing. In the following we discuss the issues relevant to each radar data dimension.

The image grating lobes (also known as “ambiguities” in the radar literature<sup>11</sup>) are a very serious artifact of radar signal processing, which manifests itself as false replicas of a target response showing at incorrect spatial locations. One basic rule in designing the SAR system parameters is to choose radar data sampling rates that ensure unambiguous ranges larger than the image size in all spatial dimensions. However, following this design rule alone does not completely solve the grating lobe issue, since targets placed outside the image domain can always create ambiguous responses that fold back inside the image volume. Consequently, additional grating lobe suppression techniques have been developed by the radar engineering community. Although a discussion of these techniques is outside the scope of this study, Section 3.5 demonstrates that the FLSAR configuration naturally leads to significant attenuation of the grating lobes in the cross-range dimension.

In terms of radar data in the frequency domain, the main limitation is linked to the signal bandwidth, which is proportional to the required time domain sampling rate. The current state-of-the-art analog-to-digital converters (ADCs) providing sampling rates in the gigasample-per-second range are still expensive. Nevertheless, radar system implementations using linear frequency modulation (LFM) and stretch processing<sup>12</sup> can overcome this issue by lowering the required sampling rate to hundreds of megasamples per second. Additionally, the data can be sampled in the frequency domain as finely as needed to push the range

ambiguities outside the region of interest for our imaging process (a design example is shown in Section 6 of this report). Since the available signal bandwidth is not a major limitation, we can easily afford to use a tapered amplitude window in the frequency domain to reduce the downrange sidelobes while still maintaining adequate resolution in this dimension.

The length of the synthetic aperture created by the forward platform motion ( $L_x$ ) can, in principle, be extended to improve the elevation resolution. Unfortunately, due to the squinted imaging geometry, large variations in  $L_x$  translate into relatively small variations of the elevation integration angle, or elevation resolution. The baseline scenario discussed in Section 3.2 achieves 25-cm resolution in the  $z$  direction with a reasonable synthetic aperture length. The aperture can also be extended and its amplitude tapered to reduce the sidelobe levels. As discussed in Section 3.1, the  $z$ -directed resolution depends on the voxel height—the closer this is located with respect to the ground plane, the better the resolution. One way to improve this metric is to fly the aircraft at higher altitude; however, the radar platform altitude may be limited by flight dynamics constraints.

The grating lobes in elevation should not present a major issue for this imaging configuration for the following reasons. First, the presence of the ground plane ensures there are no scatterers for  $z < 0$ . Second, we do not expect any major scatterers at an elevation of more than 12 m (which is the unambiguous elevation range  $D_z$  in our baseline scenario). The absence of major scatterers outside the image frame in elevation means that we do not expect spurious grating lobes folding inside the image volume in this physical dimension. Additionally, increasing the spatial sampling rate of the synthetic aperture can be achieved in a straightforward manner by ramping up the effective pulse repetition frequency (PRF).

The most problematic radar data dimension is that of the physical aperture provided by the linear antenna array. The array width is limited by the physical width of the helicopter fuselage to no more than approximately 2 m. This puts a severe limitation on the achievable cross-range resolution. The only levers available to push this metric below 30 cm are to either operate the radar at higher frequencies (such as in the W-band), or to collect the data at closer range.

In terms of spatial sampling rate, the conventional  $\frac{\lambda}{4}$  spacing rule between antenna elements that guarantees the absence of grating lobes<sup>11</sup> is infeasible for this system: at Ka-band, that would mean 800 elements in the array, and their close spacing would lead to poor gain and mutual coupling issues. Therefore, the only solution is to relax the element spacing requirement and deal with the presence of grating lobes by other methods. Fortunately, as suggested by the graphs in Fig. 10b, the

cross-range grating lobes are clearly suppressed with respect to the main lobe (by 14 dB in that numerical example). This feature is specific to the FLSAR system and is explained in more detail in Section 3.5.

The cross-range sidelobes cannot be easily suppressed by aperture tapering because that would increase the main lobe width or decrease the cross-range resolution, which is fairly limited to start with. Therefore, other techniques must be used to address this issue. A sidelobe reduction method called the recursive sidelobe minimization (RSM) is explored in Section 3.6 of this report.

One aspect of the radar data not discussed so far in this section is the computational load created by moving these data between various system blocks and processing them in the image formation algorithm. The implementation of both system hardware and computationally efficient image formation algorithms is outside the scope of this work and will be investigated in future studies. Nevertheless, the amount of data throughput and processing must be taken into account when designing the radar system. This is particularly important for a low SWAP-C sensor that is supposed to be installed onboard an aircraft and operate in real time.

### **3.5 Effect of Along-Track Integration on Grating Lobes**

---

As demonstrated in Figs. 5f and 10b, the level of the first-order grating lobes in cross-range is about 14 dB below the main lobe magnitude. This result is different from the theory of stationary linear antenna arrays, which predicts the existence of grating lobes equal in magnitude with the main lobe.<sup>11</sup> In this section, we show that the grating lobe attenuation is an effect of the forward (or along-track) integration taking place in the FLSAR system.

To illustrate this effect, we begin by presenting the 3-D SAR images obtained by a system equipped with a fixed linear antenna array (no forward motion involved). The array dimensions and element spacing are the same as in the previous examples: horizontal range is  $X_a = 150$  m and height is  $Z_a = 26$  m. The images are shown in Fig. 11, plotted in the principal Cartesian planes (Figs. 11a, 11c, and 11d) and on the sidelobe sphere discussed in Section 3.3 (Fig. 11b). One obvious feature visible in these images is the lack of resolution in the vertical direction, especially when we look along the circle in the  $x$ - $z$  plane going through the origin. Less obvious but nevertheless important image features are the grating lobes along the cross-range sidelobe lines on the sphere's surface, equal in magnitude with the main lobe in the origin. These are represented graphically by the green line in Fig. 12.

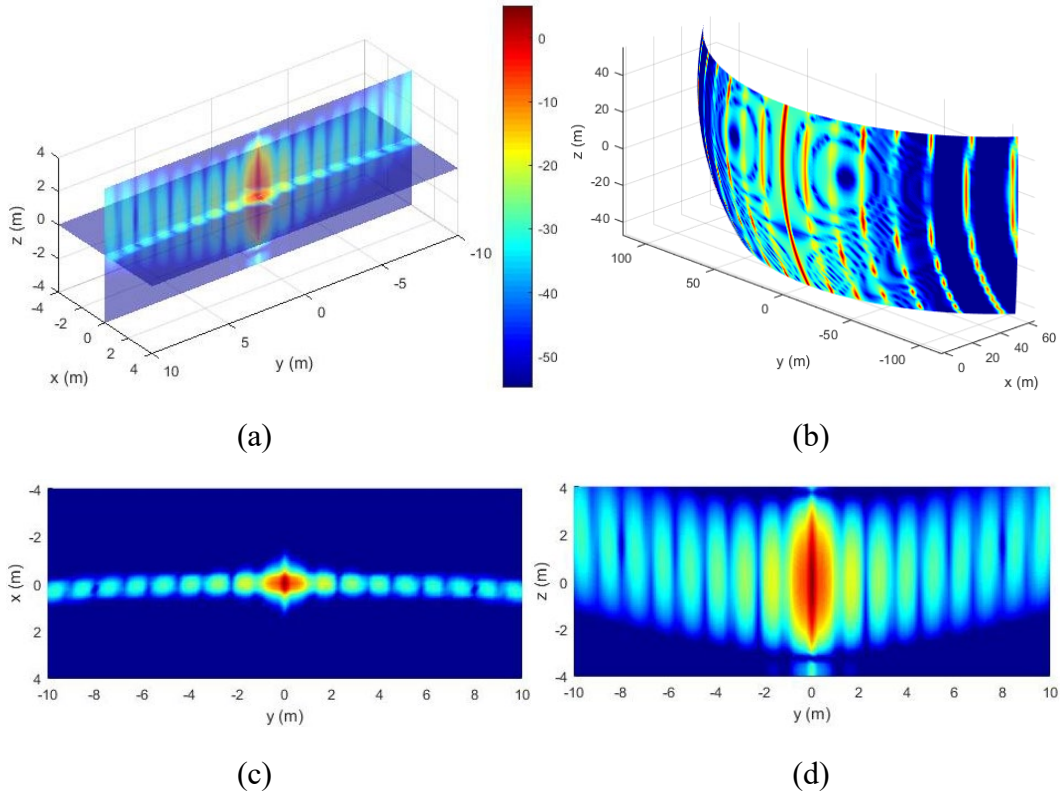


**Fig. 11** Graphic representation of the PSF for a fixed antenna array, with the point target placed in the origin of the coordinate system: a) x-y and y-z planes, perspective view; b) painted on the surface of the sidelobe sphere; c) x-y plane; and d) y-z plane

Next we consider data from additional along-track aperture positions in creating the SAR image. In these simulations, we always “fill in” a forward synthetic aperture of length  $L_x = 15$  m by increasing the number of in-between positions (or  $x$ -directed samples) from 2 to 16. The magnitudes of the resulting image voxels along the cross-range sidelobes curves are plotted in Fig. 12, for configurations involving 1, 2, 4, 8, and 16 along-track samples.

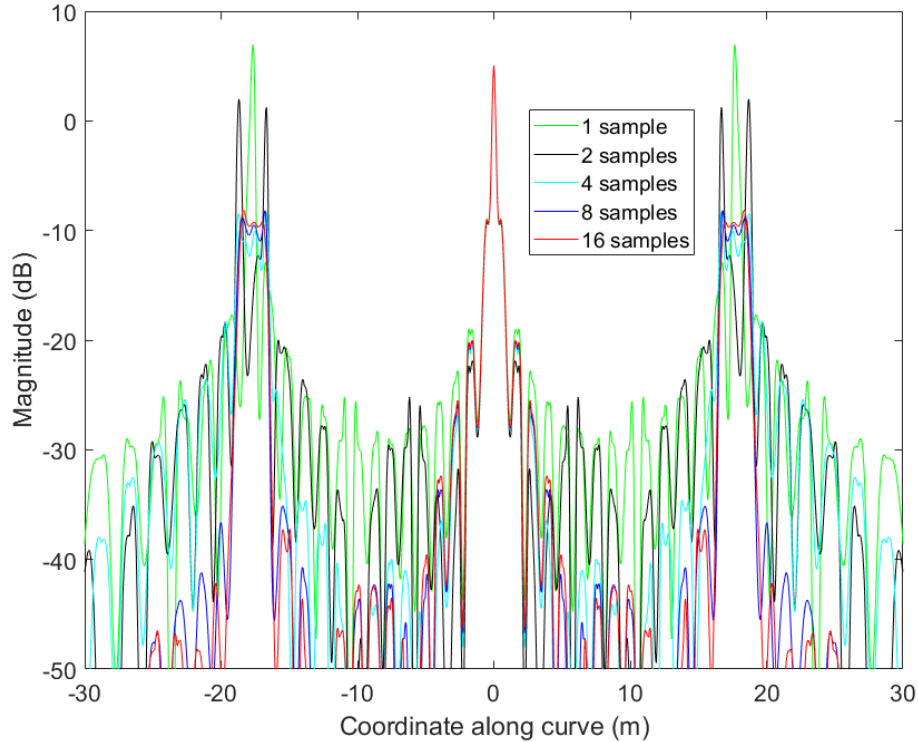


**Fig. 12 Magnitude of the image voxels along the sidelobe lines for various numbers of along-track synthetic aperture samples, showing the variation of the first-order grating lobes for abscissa equal to  $\pm 18$  m.**

As expected, when we consider a single fixed array position (one sample), the grating lobes are as large as the main lobe (5 dB). When we increase the number of along-track positions of the array, the grating lobes start to attenuate. However, it is apparent that beyond a certain number of samples (in our case, four), the grating lobe level remains basically constant at about  $-9$  dB.

A qualitative explanation for this phenomenon goes as follows: each along-track position of the array adds a contribution to the image voxel at the grating lobe location, which has different phase compared to the other along-track position contributions. Averaging these noncoherent contributions (as complex numbers) results in a voxel magnitude that is clearly below that of the main lobe, where the contributions always combine coherently. Nevertheless, in order for the phase scrambling process to occur at the grating lobe location, the radar-target range differences between various array positions must be sufficiently large. A quantitative analysis shows that this phenomenon starts to occur when the spacing between successive along-track positions satisfies  $\Delta x \geq \frac{X_a}{N}$ , where  $N$  is the number of elements in the antenna array. Furthermore, the maximum grating lobe

magnitude attenuation due to the along-track integration is  $A_{\max} = \frac{L_x N}{X_a}$  (note that

this figure is independent of  $M$ , the total number of along-track positions). For our FLSAR parameters, we obtain  $A_{\max} = 14$  dB, which is exactly the limit achieved in Fig. 12 as well as in the plots in Figs. 5f and 10b.

To further confirm the grating lobe attenuation formula, we consider different along-track synthetic aperture lengths, this time fully sampled in the  $x$  direction. Thus, Fig. 13 shows the variation of the grating lobe magnitude with  $L_x$ , demonstrating that for every doubling in forward aperture length, the attenuation doubles as well (or the magnitude goes down by 6 dB). This analysis clearly indicates that to suppress the cross-range grating lobes we can 1) increase the length of the along-track synthetic aperture, 2) increase the number of antenna elements in the array, or 3) operate at shorter ranges.

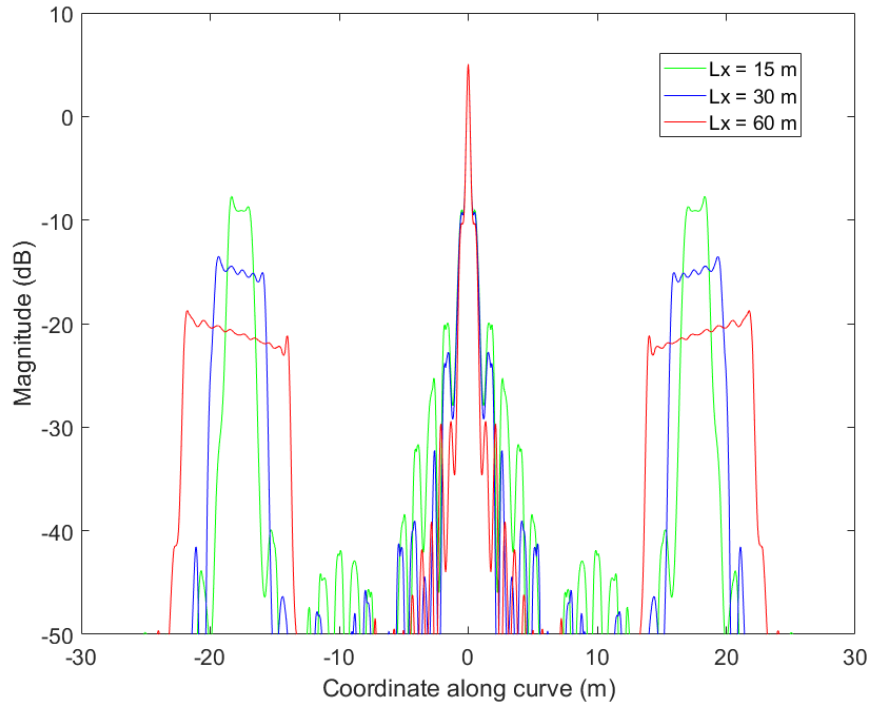


**Fig. 13** Magnitude of the image voxels along the sidelobe lines for different synthetic aperture lengths, showing the variation of the first-order grating lobes for abscissa equal to  $\pm 18$  m

Although not shown here, the higher-order cross-range grating lobes (visible, for instance, in Fig. 11b) are less of a problem than their first-order counterparts. In particular, the maximum attenuation for a grating lobe of order  $N_{GL}$  is, theoretically,

$$A_{\max} = N_{GL} \frac{L_x N}{X_a}$$

be 6 dB below the first-order one, or 20 dB below the main lobe.

It is important to emphasize that the criterion  $\Delta x \geq \frac{X_a}{N}$  does not provide a practical rule to set the sampling intervals  $\Delta x$  of the synthetic aperture. In reality, setting this sampling step is based on the desired unambiguous range in elevation, according to the formula  $D_z = \frac{\lambda R_a}{2\Delta x \sin \theta_a}$  (note that we did not consider the grating lobes in the elevation direction in this section's analysis). Since this sampling step is practically always smaller than  $\frac{X_a}{N}$ , we guarantee that the grating lobe attenuation limit established in this section is always achieved.

Considering the effects of along-track integration in the FLSAR system also includes analyzing the level of sidelobes located close to the main lobe. As shown in the graphs in Fig. 14, the addition of more synthetic aperture positions (samples) within the same aperture length  $L_x$  does not contribute much to suppressing the first-order sidelobes, which are the largest artifacts in the vicinity of the target location. However, as clearly visible in Fig. 13, extending the synthetic aperture length  $L_x$  does have a significant effect in attenuating the close-in sidelobes. Another effective technique to reduce these sidelobes without making use of aperture tapering is discussed in the next section.

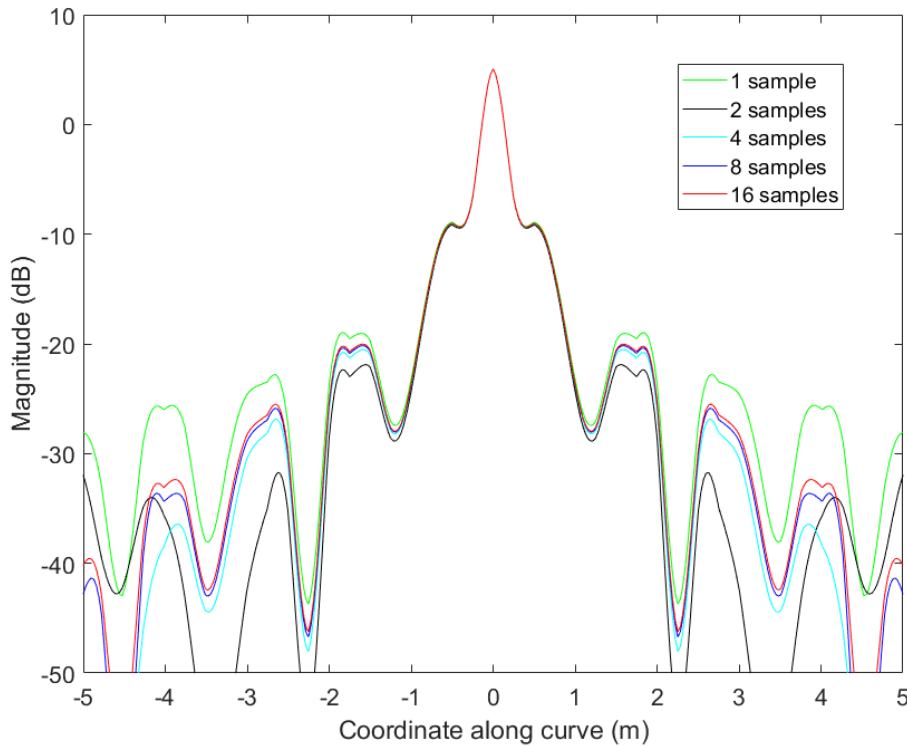


**Fig. 14** Magnitude of the image voxels along the sidelobe lines for various numbers of along-track synthetic aperture samples, showing the variation of the close-in sidelobes

### 3.6 RSM Technique for Sidelobe Suppression

---

The RSM technique was introduced by ARL researchers<sup>17,18</sup> as an efficient approach to SAR image sidelobe reduction without affecting the image resolution. In this section, we apply this technique in an attempt to suppress the cross-range sidelobes of the PSF for the FLSAR system under investigation.

The RSM algorithm is based on an iterative procedure, whereby at each iteration  $i$ , we select a random subset of the original radar aperture samples, form a new SAR image and, for each voxel location  $(x, y, z)$ , perform the following operation involving the new and old voxel complex values:

$$I_i(x, y, z) = \arg \min \left\{ |I_i(x, y, z)|, |I_{i-1}(x, y, z)| \right\}. \quad (26)$$

In this equation the  $\arg$  symbol refers to the modulus (or absolute value) operator, meaning we pick the complex value of the voxel with minimum magnitude between the two choices. The idea behind this algorithm is that the image sidelobes vary randomly with the subset of aperture samples, whereas the main lobe remains the same regardless of how we choose this subset. In the end, the voxel magnitudes at sidelobe locations are pushed down to the lowest value among all sample subsets, while maintaining the main lobe untouched.

There are two parameters for this algorithm: the percentage of aperture samples retained from the original data collection at each iteration and the total number of iterations. Note that the performance of the RSM algorithm is not entirely understood from a theoretical standpoint, and optimizing these two parameters is typically done empirically based on numerical experiments. Additionally, no quantitative iteration-stopping criterion based on image metrics is available at this time, meaning that computer simulations must be performed to determine the total number of iterations prior to applying the algorithm to a given scenario. An example of random sample subset of the 2-D aperture characteristic to the FLSAR is shown in Fig. 15. In this figure we represent the locations of the full set of aperture samples to the left and those of the random subset (80% of the original samples) to the right.

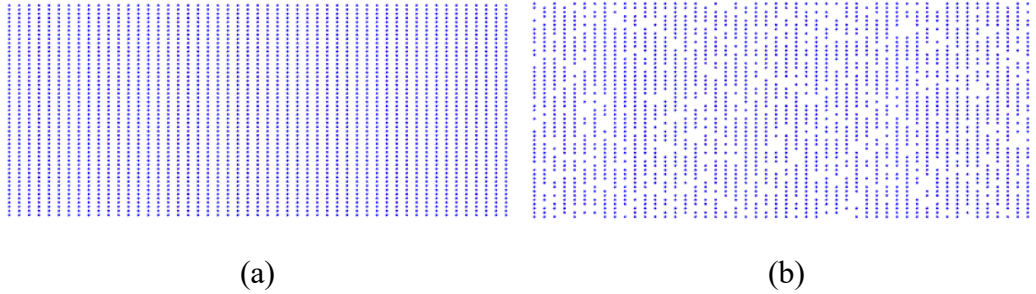


**Fig. 15 Representation of the 2-D aperture sample locations in the horizontal plane: a) the full set of samples and b) a random subset of those samples (80% of the original). Note that the figure is not to scale; its only purpose is to illustrate the principle of the RSM algorithm.**

For our FLSAR imaging geometry, the following two strategies for applying the RSM procedure are possible:

- Select a random subset of the entire 2-D aperture sample collection at each iteration, build the SAR image based on this data, and perform the voxel selection operation in Eq. 26.
- Build a set of SAR images based on one along-track aperture position at one time, applying the RSM algorithm for each of these images separately. Note that in this case we only use the radar data obtained at one fixed position of the antenna array, and the random sample subset selection is done across the array elements, in one dimension. Subsequently, we coherently combine these SAR images to obtain the final 3-D radar image.

Our numerical experiments indicated that the second procedure yielded better imaging results as measured by the level of sidelobe suppression. To illustrate this method in a qualitative manner, in Fig. 16 we plotted the PSF obtained for the same parameters as in Fig. 3 after applying the RSM technique. In this case, we used 40 iterations and retained 90% of the data at each iteration. Compared with Fig. 3 we notice that the cross-range sidelobes (along the circular arcs in the  $y$ - $z$  plane) are strongly reduced. However, the elevation sidelobes (visible in Fig. 16b) are not affected. Although the elevation sidelobe suppression was not the goal of this numerical experiment, a modified version of the procedure previously described should be able to achieve this feature as well.

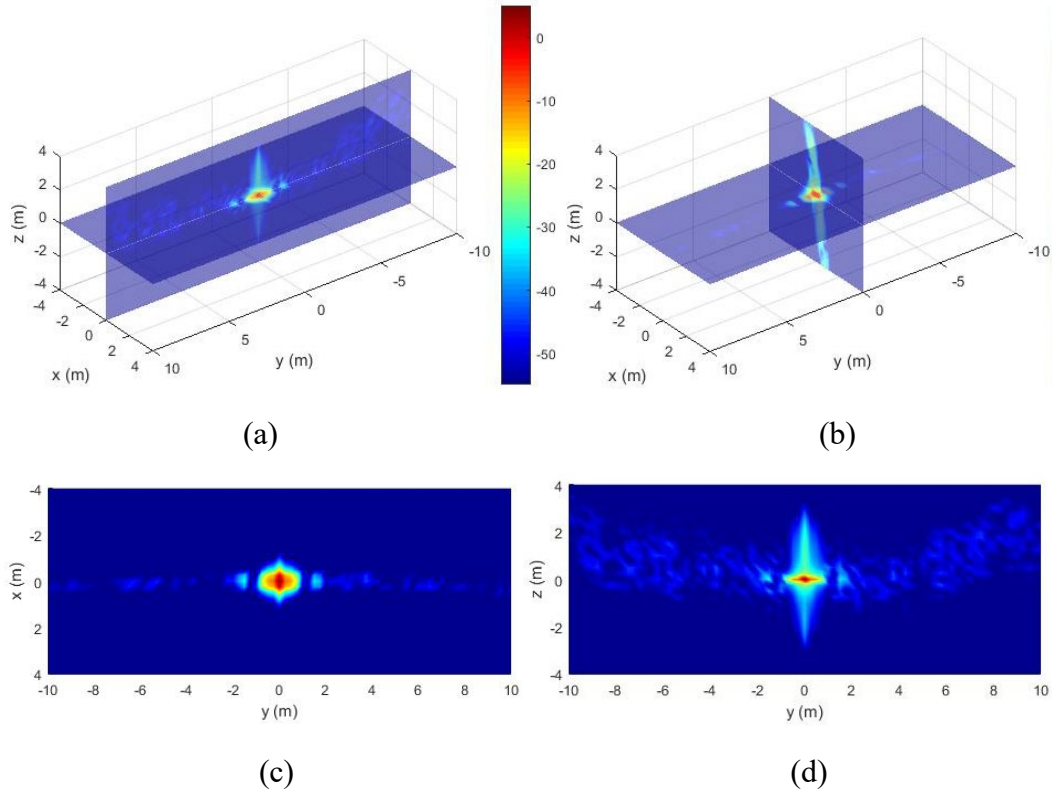


**Fig. 16** Graphic representation of the PSF for the same FLSAR parameters as in Fig. 3, after applying the RSM algorithm: a) x-y and y-z planes, perspective view; b) x-y and x-z planes, perspective view; c) x-y plane; and d) y-z plane

For a more quantitative evaluation of the RSM algorithm's performance, in Figs. 17 and 18 we plotted the magnitude of the image voxels along the cross-range sidelobe lines for different values of the algorithm's parameters. Thus, in Fig. 17 we varied the percentage of aperture sample positions retained from the original data at each iteration. This graph suggests that a larger percentage of 80%–90% produces better results (higher sidelobe suppression) than a smaller one. Figure 18 investigates the sidelobe reduction as a function of the number of iterations. It concludes that about 30 iterations are enough to reach a good level of suppression (about 20 dB). Another feature clearly visible in Figs. 17 and 18 is that the RSM algorithm is not able to reduce the grating lobes—these need to be addressed by other methods, as described in Section 3.5.

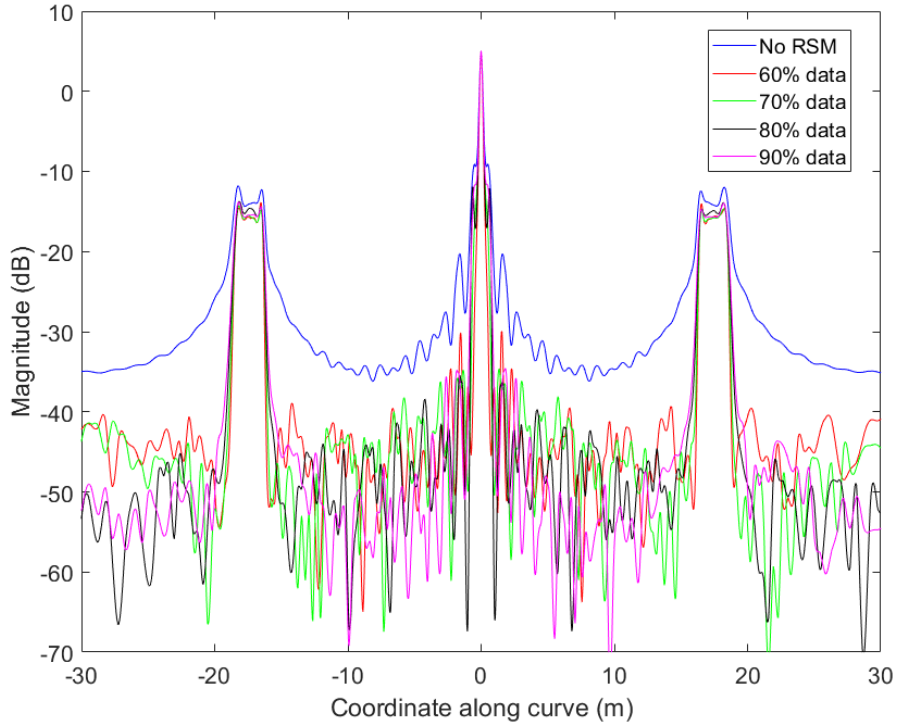


**Fig. 17** Voxel magnitude along the sidelobe line, comparing the original SAR imaging algorithm with the RSM algorithm for various data percentages retained at each iteration. In all cases, the RSM procedure uses 40 iterations.

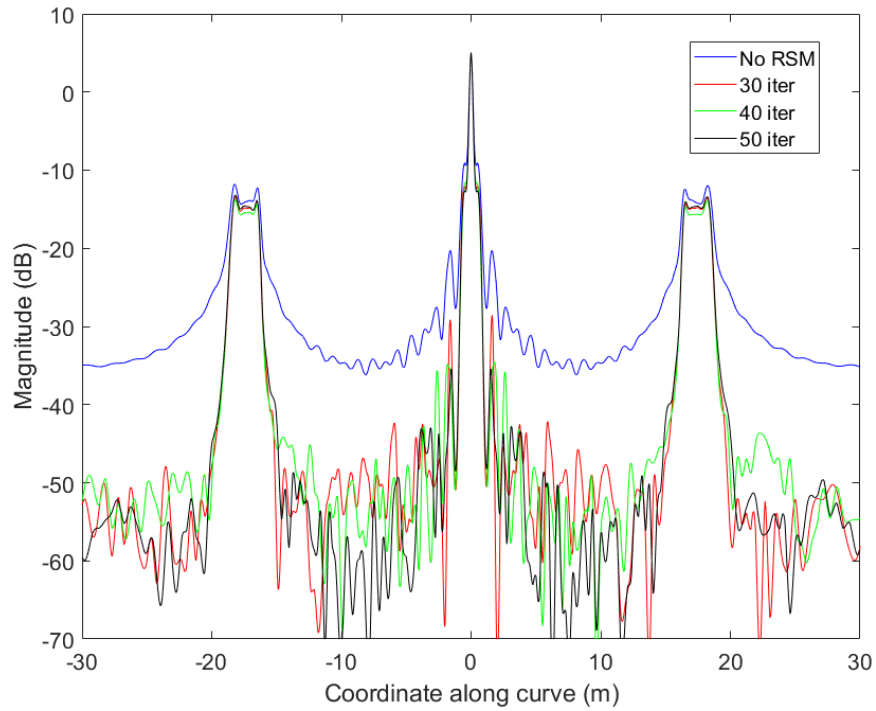


**Fig. 18** Voxel magnitude along the sidelobe line, comparing the original SAR imaging algorithm with the RSM algorithm for numbers of iterations. In all cases, the RSM procedure uses 90% of the data at each iteration.

Approved for public release; distribution unlimited.

As expected, the sidelobe reduction afforded by the RSM technique comes with an increase in computational load as compared with the basic SAR imaging algorithm. Computationally efficient implementations of the RSM algorithm have been investigated elsewhere and will not be discussed in this report (see Nguyen<sup>17</sup> for more details). As a general rule, a fast RSM implementation uses a large percentage of the data at each iteration (which may seem counterintuitive at first) and stops after just enough iterations that reach a desired level of sidelobe reduction.

#### **4. Antenna Array Configurations and Scanning Techniques**

---

As discussed in the general system description in Section 2, the FLSAR is equipped with a physical linear antenna array providing resolution in the cross-range direction. In Section 3, we assumed this antenna array as made up of an equal number of Tx and Rx elements, operating in a monostatic configuration. Although we did not make any specific assumption regarding the pulse transmission sequence, the most basic scheme, where identical waveforms are transmitted with each pulse, requires activating the Tx–Rx element pairs one by one, sequentially. This baseline antenna array configuration provides a good starting point in analyzing the radar system’s PSF. However, a practical implementation of the FLSAR will most likely use some alternative configuration designed to offer better performance at a reasonable cost. In this section, we explore several possible versions of antenna array design and discuss their pros and cons.

When choosing an antenna array design solution, the radar engineer must consider criteria such as sensing performance, operational performance, complexity, and cost. In the sensing performance metrics, we include the resolution, the unambiguous cross-range swath, and the signal-to-noise ratio (SNR). The data acquisition time is an important operational performance metric. The complexity and cost of an antenna array are largely dictated by the number of Tx and Rx elements and channels, their activation sequence algorithm, and the computational complexity involved by data processing.

In the following, we assume that the antenna array is equipped with  $N$  receiving elements. As already discussed, achieving the condition  $\Delta y \leq \frac{\lambda}{4}$  for element spacing (which would completely eliminate the grating lobes) is extremely difficult from a practical standpoint, so we assume that this criterion is not met in our scenario (the spacing is larger than  $\frac{\lambda}{4}$ ). We do not make any specific assumption about the type of antenna elements used for this design, although for MMW frequencies and small fractional bandwidths, simple-shaped patch antenna

elements are very common.<sup>19</sup> These elements provide a low-cost, low-profile, and easy-to-manufacture array solution while achieving reasonable performance in terms of gain. Higher gains can be obtained by using horn antenna elements<sup>19</sup>; however, these are more difficult to integrate in large numbers into a linear array and therefore constitute a practical solution only for designs involving a small number of Tx antenna elements.

The performance analysis in this section is focused on image metrics in the cross-range direction. That is, we ignore the radar waveform bandwidth, as well as the platform's forward motion; in effect, we consider a fixed, linear antenna array. Nevertheless, the analysis presented here is relevant to the FLSAR system as a whole, as demonstrated by the design example in Section 6.

The following is a possible (but not necessarily exhaustive) list of antenna array configurations under consideration for the FLSAR system:

- (1)  $N$  monostatic Tx–Rx pairs turned on sequentially (one pair at a time). This is essentially the configuration analyzed in Section 3 and illustrated in Fig. 19. As already discussed, the cross-range resolution at range  $R$  is  $\delta y = \frac{\lambda R}{2L_y}$ , and the

unambiguous cross-range swath is  $D_y = \frac{\lambda R}{2\Delta y}$ . The array processing SNR gain

per full scan is  $N$ ,<sup>11</sup> while the acquisition time in number of pulses per scan is also  $N$ . In terms of hardware complexity, this array requires  $N$  Tx and  $N$  Rx elements; however, since only one element pair is active at one time, we only need one pair of Tx and Rx channels equipped with RF electronics. This makes for a very low-cost system design, although building low-loss, fast-speed switches for a large number of elements (on the order of  $N = 50$ ) could prove very challenging in practice.

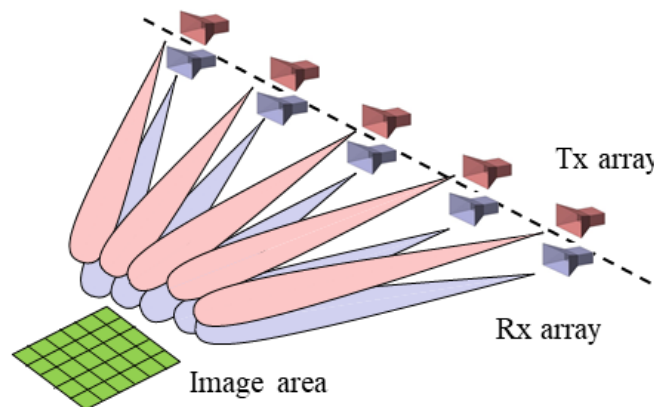


**Fig. 19 Schematic representation of Configuration 1 for the antenna array, showing the Tx antenna beams in pink and the Rx antenna beams in purple**

(2)  $N$  Rx elements combined with two Tx elements placed at the array ends, working in a slightly bistatic configuration (Fig. 20). The two Tx elements are activated sequentially, while the Rx elements can receive either one at a time or all at a time depending on how many channels are equipped with RF electronics. In the first case, we only need one active Rx channel (and a channel switching scheme similar to Configuration 1, while in the second case we need  $N$  Rx active channels, with a corresponding increase in system cost, as well as data throughput. Note that this configuration is already used in existing FLSAR systems such as SIRE or SAFIRE.

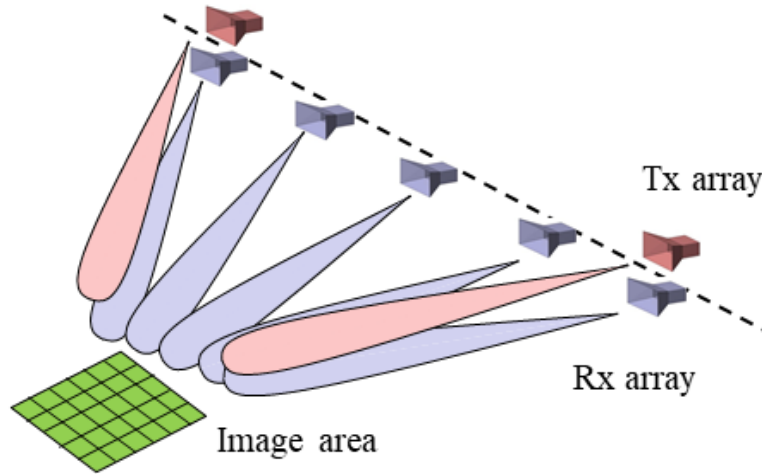


**Fig. 20** Schematic representation of Configuration 2 for the antenna array, showing the Tx antenna beams in pink and the Rx antenna beams in purple

As is well-known from the antenna array theory,<sup>20</sup> this configuration is equivalent to a fully monostatic array of the same length ( $L_y$ ) equipped with  $2N$  equally spaced Tx–Rx pairs. This result can be explained based on the observation that a bistatic radar measurement involving a small bistatic angle is approximately equivalent with a monostatic measurement at the bisector angle.<sup>21</sup> Consequently, the cross-range resolution for this configuration is

$$\delta y = \frac{\lambda R}{2L_y} \text{ (same as in Configuration 1), while the unambiguous cross-range}$$

swath doubles to  $D_y = \frac{\lambda R}{\Delta y}$  (since the equivalent monostatic array has elements

spaced at half the distance compared with Configuration 1).

Only one Tx channel needs to be active at one time (the two Tx channels are toggled sequentially), while the possible Rx channel activation schemes have already been discussed. The acquisition time in number of pulses per scan can be either  $2N$  or  $2$ , depending on how many Rx channels are active at one time,

while the SNR gain per scan is  $2N$ . When processing the radar data, we deal with twice the amount available in Configuration 1 per scan, which increases both the data throughput and the computational complexity.

- (3) A fully populated array of  $N$  Tx and  $N$  Rx elements, with the Tx elements switched sequentially (only one active at a time) and all Rx elements receiving simultaneously (refer to Fig. 19, which depicts the same physical configuration; the difference between the two cases consists in the activation sequence of the Tx–Rx pairs). Since this configuration is equivalent to a monostatic array of  $N^2$  Tx–Rx pairs within the same length  $L_y$ , it offers some excellent performance metrics: the cross-range resolution is the same as in Configuration 1, but the unambiguous cross-range swath is  $D_y = \frac{N\lambda R}{2\Delta y}$ , while the SNR gain per scan is  $N^2$ . However, this performance comes at the expense of increased hardware and computational complexity. Thus the system requires  $N$  fully equipped Rx channels, while the amount of radar data to process per scan is now  $N^2$ . The acquisition time in number of pulses per scan is  $N$ .
- (4) A fully populated array of  $N$  Tx and  $N$  Rx elements performing beamforming on both transmit and receive<sup>11</sup> and scanning the beams over the area of interest. Although this configuration is a departure from the “computational beamforming” concept, which is one of this project’s foundational ideas, it should be considered in a possible scenario where the 3-D imaging algorithm’s computational complexity becomes too large to handle in real time. This array configuration can be physically described by Fig. 19 in the sense that all the Tx and Rx elements are activated at the same time. However, an equivalent picture is shown in Fig. 21, where we depict the pairs of Tx–Rx beams obtained through the beamforming process, pointing sequentially in different directions.

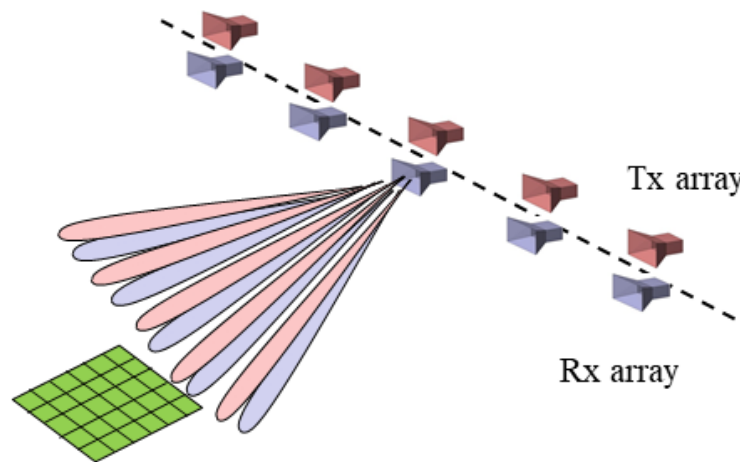


**Fig. 21 Schematic representation of Configuration 4 for the antenna array, showing the equivalent Tx beams in pink and the equivalent Rx beams in purple**

The essential insight in operating a beamforming antenna array within the FLSAR framework is that beamforming and SAR imaging with a fixed array are largely equivalent processes. This can be seen, for instance, by comparing the equations involved in SAR imaging by the matched filter method with the classic beamforming equations.<sup>11</sup> The formal difference is that in SAR imaging we typically work with Cartesian pixel or voxel coordinates, while in beamforming we work with angles. Consequently, while a SAR image is typically mapped on a rectangular grid, radar images obtained by the beamforming and scanning processes are mapped on a polar format grid.

We can also directly compare the performance of beamforming with that of the SAR imaging configurations previously considered. Thus, both the cross-range resolution and the unambiguous cross-range swath at range  $R$  are the same as in Configuration 1. The SNR processing gain per scan is  $N^2$ , while the acquisition time is  $N$  pulses (required to scan the beam through all angular positions). This system is typically expensive, because it requires all  $N$  Tx–Rx channel pairs to be active at all times, and, depending on architecture, all the Rx channels may need to be equipped with RF electronics (such as in the case of digital beamforming<sup>12</sup>). Nevertheless, the increase in hardware complexity compared with the previous configurations is compensated for by a decrease in the computational complexity of the imaging process, since computations in one dimension (cross-range) can be readily dropped out of the SAR imaging algorithm.

- (5) A fully populated, multiple-input, multiple-output (MIMO) array.<sup>22</sup> This involves  $N$  Tx–Rx element and channel pairs, all of them activated simultaneously. The  $N$  Tx send out a set of  $N$  waveforms orthogonal to one another, while each Rx channel is equipped with a filter matched to the corresponding waveform transmitted by its Tx pair. The principle is illustrated in Fig. 22, where the various beam colors designate different waveforms being transmitted and received.

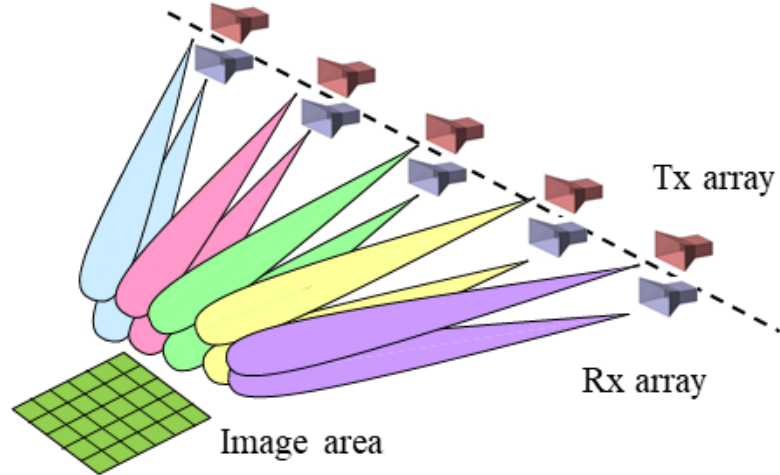


**Fig. 22** Schematic representation of Configuration 5 for the antenna array, showing the Tx–Rx beam pairs in different colors, corresponding to the waveforms transmitted on each channel

MIMO radar systems typically offer high performance matched by a high cost. Thus, the cross-range resolution and unambiguous swath are the same as in Configuration 1. However, the SNR processing gain per scan is  $N^2$ . Moreover, a full scan only takes the duration of one pulse, which makes this configuration the solution of choice for applications where very rapid data acquisition is required. The main increase in complexity comes from the fact that all Tx and all Rx channels need to be independently equipped with their own RF electronics. Additionally, finding a large set of waveforms with a good degree of orthogonality is a far from trivial issue. Most likely, a system built around a MIMO array would have to contend with a much smaller number of channels than what we considered in the previous design options.

All the performance and complexity/cost metrics discussed in this section are summarized in Table 1. In this table, the green cells mark favorable metrics, red cells mark poor metrics, and yellow cells are in-between. The “full” resolution metric refers to the formula  $\delta y = \frac{\lambda R}{2L_y}$  (valid for all cases). A “single” unambiguous

cross-range swath is  $D_y = \frac{\lambda R}{2\Delta y}$ . The SNR gain is evaluated per full array scan with

respect to a single-channel system SNR. The acquisition time is measured in number of pulses per full scan. The number of Tx and Rx channels refers to those that must be equipped with their own RF electronics, while the data amount represents the number of samples in the array dimension processed in the image formation algorithm. Regarding the relative importance of various performance metrics, one could argue that a fast acquisition time is not a critical constraint for

this FLSAR imaging system (as demonstrated by the numerical example in Section 6), while the system cost is very important within the scope of this project.

**Table 1 Comparison of various performance metrics for the five antenna array configurations considered in this section**

Metric	Config #1	Config #2	Config #3	Config #4	Config #5
Resolution	Full	Full	Full	Full	Full
Unambiguous cross-range	Single	Double	N x Single	Single	Single
SNR gain	N	2N	N <sup>2</sup>	N <sup>2</sup>	N <sup>2</sup>
Acquisition time	N	2N or 2	N	N	1
Tx channels	1	1	1	N	N
Rx channels	1	1 or N	N	N	N
Data amount	N	2N	N <sup>2</sup>	1	N <sup>2</sup>
Cost	\$	\$	\$\$	\$\$\$	\$\$\$\$

Looking at the performance table, we think that Configuration 2 for the antenna array offers a good balance among the different metrics. Since we are not primarily concerned with fast array scanning times, we can further choose the suboption where the Rx elements are scanned sequentially. This would certainly decrease the system cost, although switching between many antenna elements is a challenging problem requiring further investigation. A compromise solution is to break the overall element array into subarrays, each of them connected to an RF electronics channel, with switches selecting alternate elements within a subarray in a sequential manner.<sup>12</sup> Subarray architectures can also be considered in conjunction with Configurations 4 and 5, although these two options would always involve higher system cost.

## 5. Positioning Errors and Motion Compensation

One important requirement in collecting radar data for SAR image formation is maintaining the data coherence over a coherent processing interval (CPI) duration. In practice, this amounts to knowing the coordinates of each antenna's phase center, at the slow-time sampling instances, with a precision on the order of a fraction of the wavelength.<sup>12</sup> In principle, these coordinates can be inferred from the platform's trajectory, assuming we know its direction of travel, velocity, and acceleration. However, at MMW frequencies, very small deviations from the assumed trajectory (on the order of 1 mm, as shown later in this section) can have a large impact on the SAR image quality. Therefore, the FLSAR radar system must be coupled with a high-precision inertial measurement unit (IMU) that provides real-time positioning data synchronous with the radar data collection. In this section, we discuss the impact of positioning errors on the 3-D SAR images and, as a related topic, techniques for incorporating the navigation data into a motion compensation scheme.

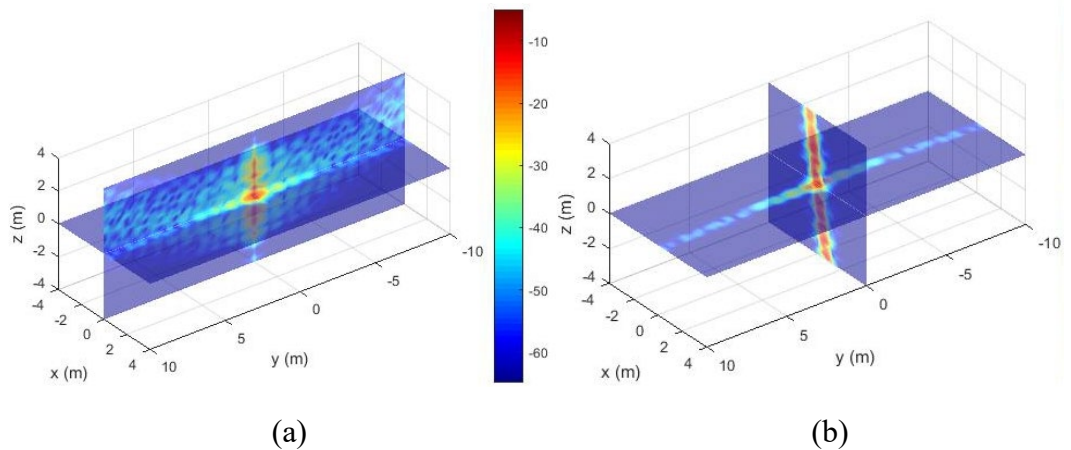
To investigate the sensitivity of the FLSAR imaging system to uncompensated positioning errors, we first need to quantify the change in the radar-voxel range caused by a position error vector  $\mathbf{r}_{mn}^e = [x_{mn}^e \ y_{mn}^e \ z_{mn}^e]^T$ . We denote by  $R_{mn}(x, y, z)$  the distance between the voxel at coordinates  $(x, y, z)$  and the radar aperture sample  $(m, n)$ , prior to introducing any positioning errors, while by  $R_{mn}^e(x, y, z)$  we denote the same distance after considering the positioning errors. In establishing a relationship between the two, we notice that the  $\mathbf{r}_{mn}^e$  vector components are much smaller (by orders of magnitude) than those of the  $(x, y, z)$  and  $(x_m, y_n, Z_a)$  vectors. Then we can apply the commonly used Taylor-series-based approximation of the square root and write

$$\begin{aligned} R_{mn}^e(x, y, z) &= \sqrt{(x_m + x_{mn}^e - x)^2 + (y_n + y_{mn}^e - y)^2 + (Z_a + z_{mn}^e - z)^2} \\ &\cong R_{mn}(x, y, z) + \frac{1}{R_{mn}(x, y, z)} [(x_m - x)x_{mn}^e + (y_n - y)y_{mn}^e + (Z_a - z)z_{mn}^e], \quad (27) \\ &= R_{mn}(x, y, z) + \frac{\mathbf{R}_{mn}(x, y, z) \cdot \mathbf{r}_{mn}^e}{R_{mn}(x, y, z)} = R_{mn}(x, y, z) + |\mathbf{r}_{mn}^e| \cos(\theta_{mn}^e(x, y, z)) \end{aligned}$$

where  $\mathbf{R}_{mn}(x, y, z) = [x_m - x \ y_n - y \ Z_a - z]^T$  is the radar-voxel position vector describing the line of sight (LOS), and  $\theta_{mn}^e(x, y, z)$  is the angle between the LOS vector and the  $\mathbf{r}_{mn}^e$  error vector.

The major insight gained from this analysis is that the positioning errors have a big effect on the radar phase measurement when they occur in a direction close to the LOS (that is,  $\theta_{mn}^e(x, y, z)$  is close to  $0^\circ$ ), and they have little impact when they occur in a direction orthogonal to the LOS (when  $\theta_{mn}^e(x, y, z)$  is close to  $90^\circ$ ). For our specific geometry, where the LOS is oriented close to the  $x$  axis, we expect positioning errors along the  $x$  axis to have a large impact on the SAR image quality. However, errors occurring along the  $y$  axis have almost no effect on the image. The errors along the  $z$  axis, for which  $\theta_{mn}^e(x, y, z)$  is about  $80^\circ$ , have some effect on the image, but this is significantly less dramatic than that occurring for the  $x$ -directed errors.

To obtain a quantitative assessment of the positioning errors' impact on the 3-D SAR image quality, we performed a series of numerical simulations of the image PSF. A clear demonstration of these effects is shown in Fig. 23, where we plot different views of the PSF obtained from measurements where we introduced a random, uncompensated positioning error with a standard deviation of 1 mm in the  $x$  direction. In generating this measurement model, we assumed the errors to be uncorrelated from one forward aperture position to the next. The fixed antenna array has the same monostatic configuration as in Section 3, or Configuration 1 in Section 4, and the ideal platform trajectory is that described in Fig. 1. The images in Fig. 23 display obvious defocusing of the SAR image, especially in the  $y$ - $z$  plane, as well as a significant reduction of the PSF peak (by about 10 dB). Evidently, these effects have a significantly detrimental impact on the SAR image quality and degrade the performance of any target detection algorithm.



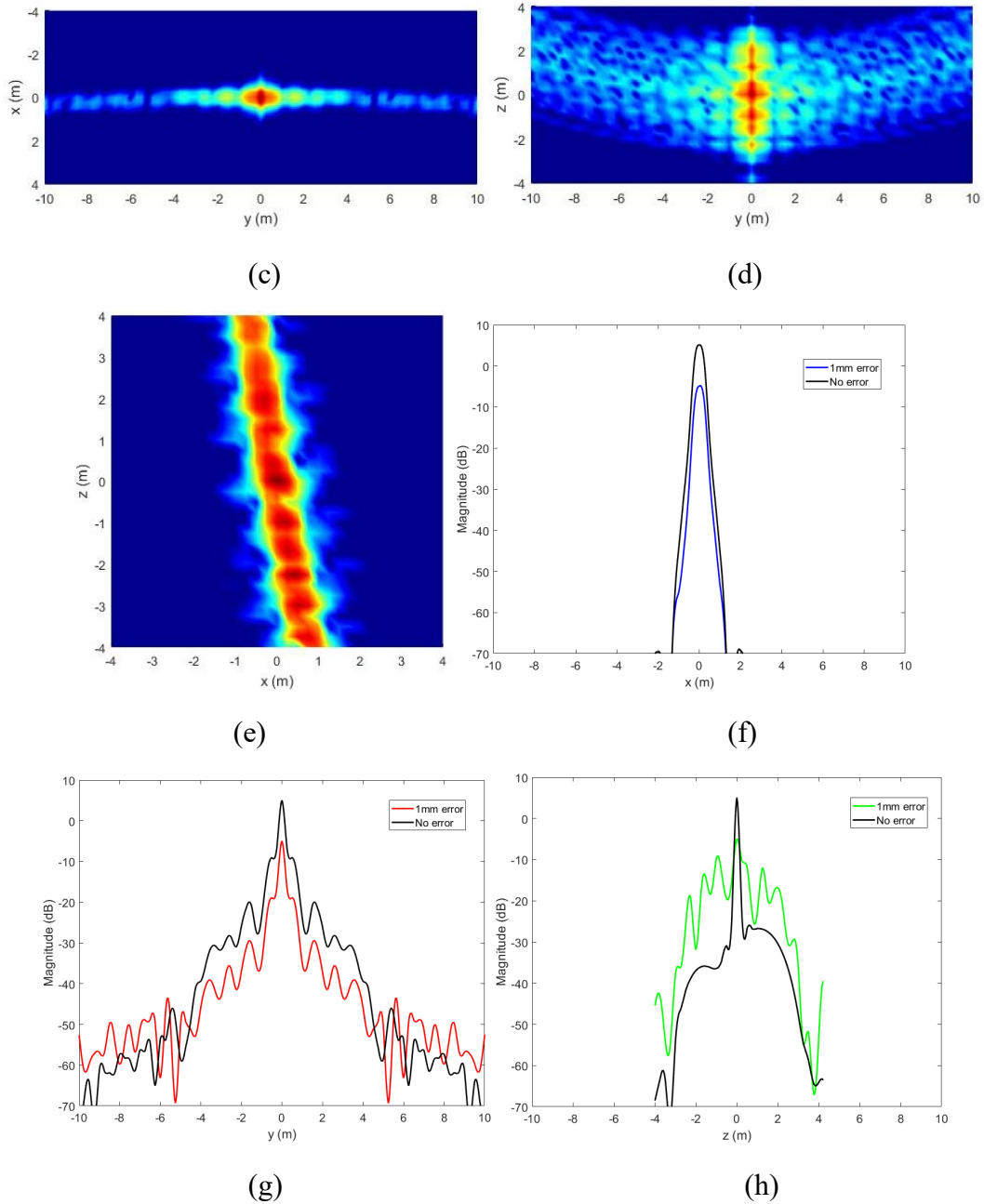


**Fig. 23** Graphic representation of the PSF with the point target placed in the coordinate system origin, after introducing a set of uncorrelated positioning errors in the x direction, with standard deviation of 1 mm: a) x-y and y-z planes, perspective view; b) x-y and x-z planes, perspective view; c) x-y plane; d) y-z plane; e) x-z plane; f) cut along the x axis; g) cut along the y axis; and h) cut along the z axis

For a more systematic image sensitivity study, we classify the positioning errors into translational errors (which may occur along one of the Cartesian axes) and rotational errors (yaw, roll, and pitch, as shown in Fig. 24). Note that we measure the yaw, roll, and pitch angles with respect to the middle of the antenna array. The diagrams in Fig. 24 intuitively suggest (and our numerical simulation confirmed)

that the pitch errors have virtually no impact on the SAR images, while the yaw errors, which are clearly related to  $x$ -directed displacements, have a very large effect on the image quality. As for the roll errors, which are more closely related to  $z$ -directed displacements, the effect is somewhere in-between. A formal description of the radar antenna phase center coordinates at aperture indexes  $(m, n)$  after introducing the displacements induced by all the positioning error types relevant to this scenario is

$$\begin{bmatrix} x_{mn}^{new} \\ y_{mn}^{new} \\ z_{mn}^{new} \\ 1 \end{bmatrix} = \begin{bmatrix} 1 & -\alpha & \alpha\beta & x_T^e \\ \alpha & 1 & -\beta & y_T^e \\ 0 & \beta & 1 & z_T^e \\ 0 & 0 & 0 & 1 \end{bmatrix} \begin{bmatrix} 0 \\ y_n \\ 0 \\ 1 \end{bmatrix} + \begin{bmatrix} x_m \\ 0 \\ Z_a \\ 0 \end{bmatrix}, \quad (28)$$

where  $(x_m, y_n, Z_a)$  are the original radar coordinates at aperture indexes  $(m, n)$ ,  $\begin{bmatrix} x_{mn}^{new} & y_{mn}^{new} & z_{mn}^{new} \end{bmatrix}^T$  is the new radar position vector at the same aperture indexes,  $\begin{bmatrix} x_T^e & y_T^e & z_T^e \end{bmatrix}^T$  is the translational error vector, and  $\alpha$  and  $\beta$  are the yaw and roll error angles in radians, respectively.

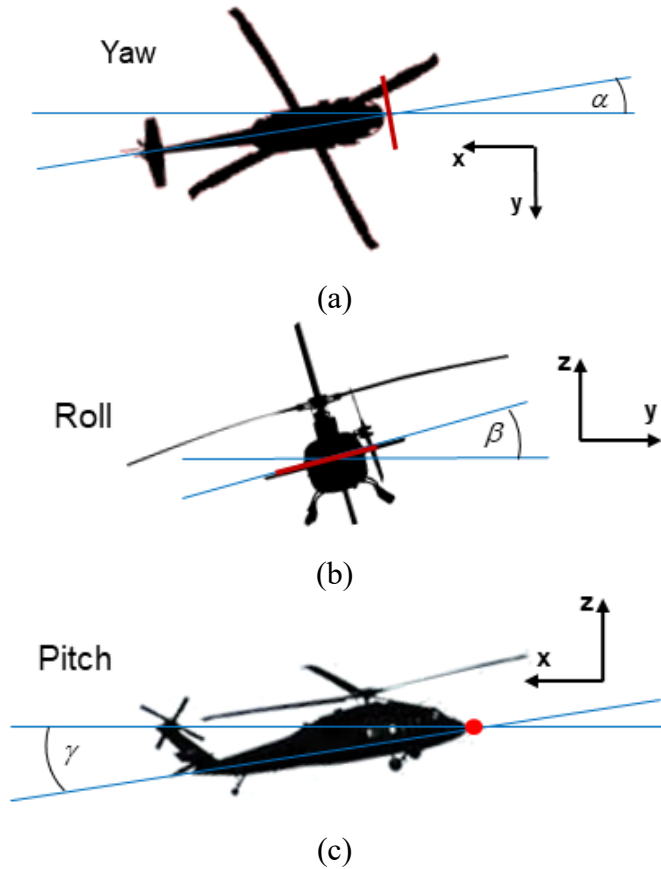


**Fig. 24** Possible rotorcraft rotational errors: a) yaw of angle  $\alpha$ , b) roll of angle  $\beta$ , and c) pitch of angle  $\gamma$

Additionally, an important aspect of the positioning error model is its dynamic behavior (i.e., its variation with time; more exactly, over the slow-time sample sequence). Accordingly, we investigated four dynamic models of the random positioning errors: 1) errors perfectly correlated over a CPI (constant errors), 2) errors partially correlated over a CPI, using an exponential correlation function over time, 3) completely uncorrelated errors over a CPI (as in the example in Fig. 23), and 4) periodic errors over a CPI. In all cases where we introduced random errors, their probability distribution function is zero-mean Gaussian. We assumed that the same extended error vector  $\begin{bmatrix} x_T^e & y_T^e & z_T^e & \alpha & \beta \end{bmatrix}^T$  applies to all antenna elements within the fixed array at one slow-time sample, which corresponds to one position of the array in the forward synthetic aperture. For brevity, here we offer only a summary of our overall findings:

- Perfectly correlated translational errors have no effect on the image, except for a possible shift of the PSF peak, which is typically much smaller than the resolution cell.
- The errors have larger impact when they occur along the radar LOS because the phase variations are the largest for displacements along this direction. That means yaw and  $x$ -directed errors have a large impact, pitch and  $y$ -directed errors have almost no impact, while roll and  $z$ -directed errors have a moderate impact on the image quality.
- The degree of correlation among errors corresponding to different slow-time samples has an impact on the image quality. The effect is largest for uncorrelated errors and tapers away as we increase the correlation time of the error vector sequence.
- For good image quality, we need to keep the root-mean square (RMS) errors along the  $x$  axis below 1 mm, while the yaw errors should be less than  $1^\circ$ .
- If the platforms flies with a constant squint (“crab angle”) or tilt and these angles are known, there is no negative impact on the images. To test this, simulations were run with squint or tilt up to  $30^\circ$ , showing no measurable changes in the images. However, there are limits to the allowable squint/yaw and pitch angles: all of these must be smaller than half the antenna element beamwidth to make sure the image volume stays within the antenna element beam.
- Platform vibrations are a very important source of positioning errors in a rotorcraft and were modeled as periodic errors in our sensitivity study. Helicopter vibrations have been studied extensively in the literature and are fairly well understood from a dynamic standpoint. A typical vibration

frequency for a hovering rotorcraft is 60 Hz. For the numerical example presented in Section 6, the slow-time sampling frequency of the forward synthetic aperture is 100 Hz. That means, for all practical purposes, the displacements induced by the vibrational motion appear as uncorrelated when sampled by the radar system in slow time. Therefore, this dynamic error model is equivalent to that of completely uncorrelated errors over time.

Figure 25 shows the variation of one image quality metric (namely, the PSF peak magnitude) with the RMS of the translational error in the three Cartesian directions. In all these simulations, we introduced uncorrelated errors across the forward synthetic aperture positions. In Fig. 25a we considered the monostatic geometry of the fixed array described as Configuration 1 in Section 4. Figure 25b shows the same graph for the slightly bistatic geometry described as Configuration 2 in Section 4. As expected, the two array configurations produce very similar results, showing major image degradation for  $x$ -directed errors as small as 1 mm, no effect for  $y$ -directed errors, and moderate effects for  $z$ -directed errors up to 5 mm. Note that the peak magnitude can never drop much below  $-8$  dB (which is 13 dB down from the unperturbed peak) because at that point it becomes undistinguishable from the image sidelobes.

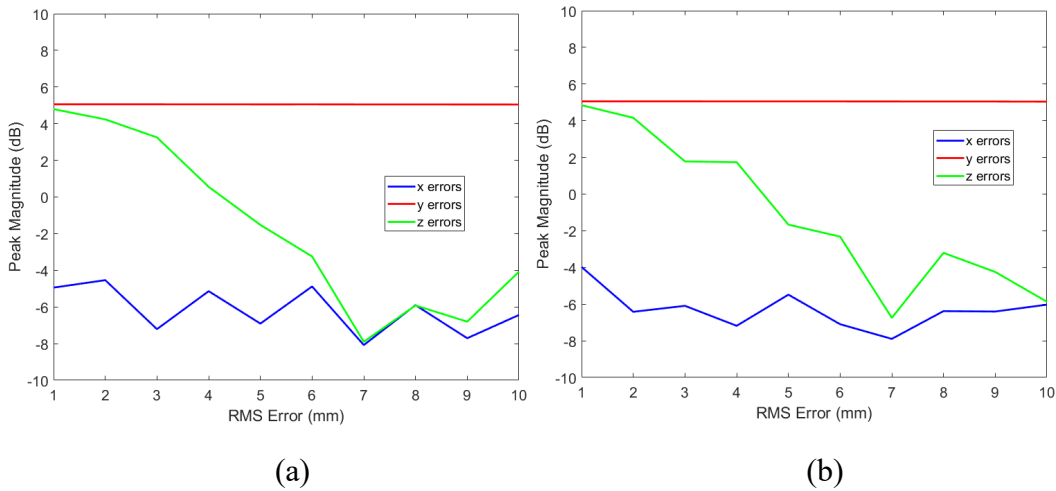


**Fig. 25** Variation of the PSF peak magnitude with the RMS of the translational errors in the three Cartesian directions: a) the monostatic antenna array described as Configuration 1 in Section 4 and b) the slightly bistatic antenna array described as Configuration 2 in Section 4

The entire discussion so far in this section assumed that all the positioning errors (translational and rotational) remain uncompensated. That means we use an assumed position vector  $\mathbf{r}_{mn} = [x_m \ y_n \ Z_a]^T$  in the imaging algorithm when the actual radar position is characterized by the vector  $\mathbf{r}_{mn}^{new} = \mathbf{r}_{mn} + \mathbf{r}_{mn}^e$ . In this scenario

the error vector quantifies our uncertainty regarding the actual radar position during the data collection. However, the radar system can be equipped with an onboard IMU measuring displacements from the ideal trajectory with better than 1-mm precision and fast update rates (on the order of kilohertz). If these displacements are known, they can be used in a motion compensation algorithm to correct for deviations from the ideal trajectory.

In the following, suppose we have already precomputed the radar-voxel distance for the ideal trajectory (i.e., the trajectory described in Fig. 1),  $R_{mn}(x, y, z)$ , and want to include the information generated by the IMU for the aperture sample  $(m, n)$  contained in the correction vector  $\mathbf{r}_{mn}^c = [x_{mn}^c \quad y_{mn}^c \quad z_{mn}^c]^T$ . To avoid an additional square root computation (as in Eq. 3), we can apply the same type of approximation as in Eq. 27 and write:

$$R_{mn}^c(x, y, z) = R_{mn}(x, y, z) + \hat{\mathbf{R}}_{mn}(x, y, z) \cdot \mathbf{r}_{mn}^c, \quad (29)$$

where  $\hat{\mathbf{R}}_{mn}(x, y, z)$  is the unit vector describing the LOS direction between the voxel  $(x, y, z)$  and the aperture sample  $(m, n)$ . At this point, we can replace  $R_{mn}(x, y, z)$  by  $R_{mn}^c(x, y, z)$  in the image formation algorithm described by Eq. 2.

To conclude this section, we emphasize that in order to compensate for the platform deviations from an ideal trajectory in the SAR image formation process, we only need to measure the displacements relative to an initial position over a CPI duration. Note that to obtain a correctly focused image, the absolute coordinates of the platform or the radar antenna elements are not required. These absolute coordinates, which can be provided by an onboard GPS are only needed in the process of SAR image registration onto the earth coordinate grid, and their required accuracy is on the order of the resolution cell size (which is much larger than a fraction of a wavelength). On the other hand, the relative coordinate displacements measured by the IMU during a CPI must be known with much better accuracy (on the order of 1 mm) to maintain coherency of the radar data. Fortunately, as shown by the numerical example in Section 6, the FLSAR system requires a relatively short CPI, typically under 1 s. During this interval, we do not expect major deviations from a preset trajectory that could not be compensated by the IMU measurements. Additionally, the short CPI ensures that the measurement drift that characterizes most IMUs over large time intervals is not a significant issue in our scenario.

## 6. System Design: Waveforms, Timing, and Power

---

In this section, we present a design case study of the FLSAR imaging system used in assisting helicopter landing in DVE conditions. Not all aspects of system design are discussed here—only the essential features related to radar waveforms, timing, and power calculations. As a starting point, we pick the same values of some system and geometrical parameters as in Section 3.2: carrier frequency (Ka-band or 35 GHz), bandwidth (500 MHz), linear antenna array width (2 m), forward synthetic aperture length (15 m), platform height (26 m), and average horizontal range (150 m). The resulting 3-D SAR images have the same resolution cell dimensions as computed in Section 3.2 ( $\delta x = 0.3$  m,  $\delta y = 0.3$  m, and  $\delta z = 0.25$  m).

For this analysis we choose Configuration 2 from Section 4 for the fixed linear antenna array configuration. That is, the array is made of  $N_t = 2$  transmitter elements placed at its ends and  $N_r = 50$  receiver elements, equally spaced along the 2-m physical aperture. We also assume that the Tx and Rx elements are scanned sequentially; that means a full array scan takes the duration of  $N_t N_r = 100$  pulses.

In terms of radar waveforms, we assume here that we use LFM (or chirp) signals for transmission. These are the most commonly used waveforms in radar systems because they can simultaneously achieve large bandwidths (for good resolution) and long durations (for high SNR). Additionally, they can be easily generated with modern RF devices such as direct digital synthesizers. To keep the sampling rate in the radar receiver within reasonable limits, a commonly used signal mixing technique is stretch processing,<sup>12</sup> whereby the received signal is mixed directly with a delayed version of the transmitted chirp and subsequently digitized. According to the theory of stretch processing, the LFM pulse width ( $T$ ), the transmitted bandwidth ( $B$ ), the sampling bandwidth ( $B_s$ ), and the unambiguous downrange swath ( $D_x$ ) are related by

$$T = \frac{2BD_x}{cB_s}. \quad (30)$$

For our design case, we choose  $B = 500$  MHz,  $B_s = 100$  MHz, and  $D_x = 300$  m. As a result, we obtain  $T = 10$   $\mu$ s.

When we talk about an unambiguous range swath of 300 m (which seems more than adequate for our application), we do not necessarily mean this swath extends from 0 to 300 m. Instead, the starting point of this range swath can be chosen arbitrarily by setting certain hardware parameters within the stretch processing scheme.<sup>12</sup>

We assume the rotorcraft platform has a velocity  $v = 30$  m/s (corresponding to 60 kt), which is a typical figure for a helicopter on a gliding path before landing. To cover a forward aperture length  $L_x = 15$  m (as in Section 3), we need an interval  $T_{CPI} = \frac{L_x}{v} = 0.5$  s. This confirms our earlier statement that the CPI required to form the 3-D SAR image is less than 1 s.

Another parameter we can evaluate is the antenna array forward displacement during one pulse transmission:  $\Delta l_x = vT$ . For the numeric values in our example, we obtain  $\Delta l_x = 0.3$  mm. While this displacement is small enough that motion compensation is not required during one pulse duration, a more serious problem is the range-Doppler coupling specific to LFM waveforms.<sup>23</sup> As is well-known from the theory of the LFM waveform ambiguity function, a relative motion between the radar platform and target with radial velocity  $v$  leads to a deviation of the estimated range of  $\Delta r_x = vT \frac{f_c}{B}$ . In our case, the ratio  $\frac{f_c}{B}$  (or the inverse of the fractional bandwidth) has a large value of 70. Consequently, the Doppler-induced error in the range estimation is  $\Delta r_x = 2.1$  cm.

Apparently, a downrange estimation error of 2 cm can be a serious issue for the 3-D SAR image formation algorithm, as suggested by the analysis in Section 5. However, as long as the platform's velocity is approximately constant, the range error is constant as well, and, as established in Section 5, a constant positioning error vector during a CPI has no impact on the SAR image. Therefore, we conclude that the issue of range-Doppler coupling in LFM waveforms should not have a significant negative effect on the FLSAR imaging system.

At this point in the design analysis a choice must be made between pulsed and continuous wave (CW) transmission. While a comprehensive discussion of the tradeoffs involved by this choice is beyond the scope of this work, the major argument favoring pulsed transmission is the isolation between the Tx and Rx antennas (since the two are activated sequentially), while in a CW system the two are turned on simultaneously (and at all times) with detrimental effects on the dynamic range. On the other hand, in a CW system, where the Tx is continuously on, the peak power required to achieve a given average power (hence, a given SNR level) is smaller than in the pulsed case. The radar system architecture using CW LFM waveforms is commonly known as frequency modulation continuous wave (FMCW) and represents a very popular solution for short-range high-resolution radar system design, including MMW SAR systems.<sup>24</sup> Both transmission schemes discussed here can accommodate stretch processing with LFM waveforms, and the pulse width calculation in Eq. 30 is valid for both options.

First, we consider an FMCW system with the design parameters calculated so far. For such a system, we have  $\text{PRF} = \frac{1}{T}$ , or  $\text{PRF} = 100$  kHz. Related to this figure, we need to verify that the second-time-around unambiguous range swath given by the formula  $D_u = \frac{c}{2\text{PRF}}$ <sup>11</sup> is larger than  $D_x = 300$  m obtained in a previous paragraph. Since  $D_u = 1500$  m, this condition is indeed satisfied.

The total number of pulses transmitted during a CPI is  $N_p = T_{\text{CPI}}\text{PRF}$ , or 50,000 pulses per CPI. Since we already established that a full array scan takes 100 pulses, this means that we need to perform 500 array scans during a CPI. While this is certainly not an impossible task for the radar hardware in terms of data throughput, the resulting large amount of data may overwhelm the processor performing the image formation algorithm. At the same time, such fine sampling of the synthetic aperture in the forward direction is probably not necessary from an image quality point of view, as discussed in Section 3.

A more reasonable solution to the antenna array activation sequence is to integrate 10 successive pulses for the same Tx–Rx antenna pair before moving to the next pair. This way, the switching between two different Tx–Rx pairs takes place every 100  $\mu\text{s}$ , and we end up with 50 full array scans during a CPI (which is a figure in line with the parameters in Section 3). Importantly, the pulse integration procedure (which we assume is done digitally) must account for the platform motion during the 10-pulse transmission interval, which amounts to 3 mm in downrange and can negatively impact the data coherency if left uncompensated. In general, given the continuous platform movement during a CPI, motion compensation must be performed more or less for every slow-time data sample that contributes to the SAR image formation. While a simple procedure to integrate the IMU data was suggested in Section 5, further investigations into fast motion compensation algorithms will likely be necessary given the real-time imaging requirements for the FLSAR system.

The second option considered in this section is that of a pulsed LFM radar system. For simplicity, we assume a duty cycle  $d_c$  of 10%. In that case, the PRF becomes 100  $\mu\text{s}$  and we end up with 50 full array scans during a CPI (no pulse integration is performed in this case). This design option leads to timing calculations very similar to the CW case; the only major difference is in the peak power required to obtain the same SNR, as shown in the following paragraphs.

The radar equation allows us to link the transmitted power and other system parameters to the SNR of the final radar map (which in our case is the 3-D SAR image). One of this equation's possible forms is<sup>11</sup>

$$\text{SNR} = \frac{P_t G_t G_r \lambda^2 \sigma G_P}{(4\pi)^3 R^4 k_B T_0 B_s FL}, \quad (31)$$

where  $P_t$  is the peak transmitted power,  $G_t$  and  $G_r$  are the Tx and Rx antenna element gains, respectively,  $\sigma$  is the target radar cross section (RCS),  $G_P$  is the processing gain,  $R$  is the range,  $k_B$  is Boltzmann's constant,  $T_0$  is the temperature,  $B_s$  is the radar sampling bandwidth (not to be confused with  $B$ ),  $F$  is the Rx noise figure, and  $L$  represents the system losses. Note that  $G_P$  is equal to the total number of *fast-time* samples employed during a CPI and includes the effects of both pulse compression and pulse-to-pulse coherent processing. Another form of the radar equation, more useful to our design case is<sup>11</sup>

$$\text{SNR} = \frac{P_a G_t G_r \lambda^2 \sigma T_{CPI}}{(4\pi)^3 R^4 k_B T_0 FL}. \quad (32)$$

Note that in Eq. 32 we used  $P_a$  (the average transmitted power) instead of  $P_t$ . The relationship between the two is  $P_a = P_t d_c$ . Let  $P_a = 10$  W, which is a fairly low average power figure that can be easily achieved with off-the-shelf power amplifiers without requiring complex cooling solutions. For a CW system ( $d_c = 1$ ) this implies  $P_t = 10$  W as well. However, for a pulsed system with  $d_c = 0.1$  we need  $P_t = 100$  W.

Numeric models of the radar scattering from terrain features of interest to this applications indicate that we need to be able to detect objects with an RCS of  $\sigma = -10$  dBsm. For the antenna gains, reasonable numbers are  $G_t = 20$  dBi (assuming horn Tx antenna elements) and  $G_r = 7$  dBi (assuming patch Rx antenna elements). The noise figure and system losses depend on the particular hardware design and components chosen for this sensor and cannot be precisely known in advance. However, a realistic assumption for the product of the two is  $FL = 13$  dB.

After crunching the numbers in Eq. 32 we obtain  $\text{SNR} = 20$  dB at a range  $R = 1000$  m. This is typically a satisfactory figure for reliably detecting targets in the presence of thermal noise (the classic detection theory for nonfluctuating targets predicts a 95% probability of detection and a  $10^{-6}$  probability of false alarm when  $\text{SNR} = 13$  dB<sup>11</sup>). Significantly better SNR performance can be achieved at shorter ranges, which would be typical for this sensor. If any system or environmental parameters need to change in this calculation, Eq. 32 contains all the relevant information to recompute the SNR for the new scenario. Keep in mind that given a specific radar frequency band and integration time, the radar designer has the following levers available to increase the SNR performance: the antenna element gains, the transmitted power, the noise figure, and the system losses.

The calculations in this section are meant primarily to give the designer a first idea of the basic radar system parameters and do not represent a complete picture of this system's performance. For a comprehensive analysis, one would need to characterize the clutter specific to the sensing scenario and, related to that, the target-to-clutter ratio, and other sources of image artifacts such as multiplicative noise (sidelobes and grating lobes) and speckle.<sup>11</sup> These calculations are outside the scope of this work and will be addressed by future studies.

This design case study is far from representing the only possible solution for the FLSAR system investigated in this report. Particularly, many other activation sequences can be devised for the linear antenna array elements, some of them possibly leading to different design parameters. Additionally, the choice of radar waveforms need not be fixated on LFM pulses. Pseudo-random phase-modulated waveforms should also be investigated as alternatives; these have the advantage of offering a low probability of intercept. On the downside, the pulse compression for these radar waveforms would require a classic matched filter,<sup>11</sup> which is typically more demanding than stretch processing on the hardware components, particularly the ADC.

Nevertheless, the numeric example presented here is a good starting point for any future hardware design effort within the scope of this project. Regardless of the particular choices made by the radar system designers, they will have to be guided by the following principles:

- The FLSAR system's cost must be affordable, which means trying to use off-the-shelf components or subassemblies as much as possible while avoiding high-performance custom-built components.
- The main thrust behind the FLSAR design is replacing the hardware complexity of conventional scanned array radar systems with the "computational beamforming" performed by the image formation algorithm.
- The system must produce high-quality 3-D SAR images in quasi-real time, meaning that data throughput and the computational complexity are very important factors in the overall system design.

## **7. Conclusions**

---

---

This report presented an analysis of the FLSAR system for helicopter landing in DVE conditions, currently under design at ARL. The emphasis was on techniques and performance metrics related to the 3-D SAR image formation process, which is the main function performed by this radar sensor. To illustrate these techniques

and quantify the metrics, we investigated the PSF of the radar imaging system for typical configurations and design parameters.

After presenting the relevant sensing geometry and image formation algorithm, we studied the most-important image quality metrics: resolution, sidelobes, and grating lobes. The investigation included both analytic formulations and numerical examples, illustrated by numerous 3-D graphic representations. We paid particular attention to the image sidelobes by performing a sophisticated 3-D geometrical analysis to obtain an accurate evaluation of these image artifacts.

A separate section was dedicated to the various performance tradeoffs involved in this system's design as well as possible ways to improve the SAR image metrics. One conclusion was that the most critical dimension of the radar data is that of the fixed antenna array, where physical constraints lead to severe limitations in terms of cross-range resolution, as well as sidelobes and grating lobe levels. Further analysis showed that the cross-range grating lobes are partially attenuated by the forward integration inherent to the FLSAR system. Also, the RSM technique for sidelobe suppression was discussed as an effective way to reduce the sidelobes without affecting the image resolution.

Next we presented several options for the fixed antenna array configuration and scanning sequence. After evaluating the pros and cons of these options in terms of imaging performance, hardware and computational complexity and cost, we suggested that a Tx-Rx configuration similar to that used in the SIRE and SAFIRE radar systems (i.e., full array of Rx elements and two Tx elements at the array's ends) may be the best solution for this design.

A critical aspect of SAR imaging systems is the coherence of the radar data collection, and, related to that, the accuracy of the platform positioning data. Section 5 of this report presented a detailed investigation of the system's sensitivity to positioning errors by considering both translational and rotational deviations from an ideal trajectory with different dynamic models. The main conclusion from this analysis is that positioning errors along the radar LOS have the largest impact on the image quality. For a radar system working at MMW frequencies, the RMS errors along this direction must be kept to less than 1 mm. We envision the addition of an onboard IMU that can provide high-precision positioning data to be used as corrections from the ideal trajectory in a motion compensation algorithm.

Finally, this report included a design case study for the FLSAR system to be used as practical guidance by the hardware engineering team in designing and building the sensor. The main aspects discussed were the radar waveforms as well as the timing parameters and power calculations. It was assumed that the radar uses LFM waveforms combined with stretch processing, although more-complex waveform

transmission schemes could be accommodated as well. One important conclusion was that the SAR system will require relatively short CPIs (less than 1 s), which makes the motion compensation schemes somewhat easier to implement. Another positive outcome of the analysis is that the FLSAR can operate with relatively low average power, about 10 W, for satisfactory SNR performance. It is not clear at this point whether the actual sensor will use pulsed or CW transmission: the choice between these two options will probably be dictated by additional hardware constraints.

Multiple issues related to the FLSAR system design remain and will have to be addressed by future efforts. In terms of SAR imaging, it is currently unclear whether the information provided by the navigation systems (primarily the IMU) will be sufficient for correct image focusing. If that proves not to be the case, SAR autofocusing algorithms<sup>25</sup> should be explored for this application. Equally important, this SAR system will be required to provide 3-D images in real time (with a lag of no more than several seconds), which may prove very challenging given the large amount of data involved in the image formation algorithm. Therefore, designing fast 3-D SAR imaging algorithms, possibly running on graphics processing unit hardware, will be another important research topic. A possible fertile avenue for the imaging procedure is that of fast Fourier transform-based algorithms, which have already been applied to 3-D imaging using MMW radar systems.<sup>26</sup> Also, efficient SAR algorithms for LFM-based systems exist<sup>24</sup> and should be explored for this application.

The hardware realization of the FLSAR system raises additional challenges. Given the high degree of maturity of current MMW RF electronics, a choice must be made between a custom hardware design and existing commercial solutions. The antenna array should accommodate as many elements as possible for a given length; however, the number of elements is constrained by multiple issues (gain requirements, electromagnetic coupling, manufacturing, cost, etc.) that will have to be addressed by the antenna designers. Integrating the navigation equipment with the radar hardware and the signal processing algorithms will be an important factor in the project's successful outcome, as will be the mechanical and aerodynamic aspects of mounting the radar antenna array on the aircraft's fuselage. In the end, our goal is to deliver a high-performance low-SWAP-C radar sensor prototype as a first step in fulfilling this critical Army modernization priority.

## 8. References

---

1. Albery W, Cheung B, Priot A-E, Kielhorn P, Kolletzki D, Münsterer T, Klein O, Nur E, de Graff M, Groen E et al. Rotary-wing brownout mitigation: technology and training. Neuilly-Sur-Seine Cedex (France): North Atlantic Treaty Organisation; 2012 Jan. Report No.: TR-HFM-162.
2. Mangogna A, Symosek P, Rapoport R, Haissig C, Ihlein J, Kazi S. Obstacle avoidance system trade study for the autonomous unmanned combat armed rotorcraft. Morris Plains (NJ): Honeywell International; 2003 Jan.
3. Rangwala M, Wang F, Sarabandi K. Study of millimeter-wave radar for helicopter assisted landing system. *IEEE Antennas and Propagation Magazine*. 2008;50(2):13–25.
4. Martin C, Kolinko V, Otto G, Lovberg G. Flight test of MMW radar for brownout helicopter landing. *Proc SPIE*. 2012;8362.
5. Ressler M, Nguyen L, Koenig F, Wong D, Smith G. The ARL synchronous impulse reconstruction (SIRE) forward-looking radar. *Proc SPIE*. 2007;6561.
6. Phelan B, Ranney K, Gallagher K, Clark J, Sherbondy K, Narayanan R. Design of ultra-wideband (UWB) stepped-frequency radar (SFR) for imaging of obscured targets. *IEEE Sensors Journal*. 2017;17(14).
7. Kositsky J, Cosgrove R, Amazeen C, Milanfar P. Results from a forward-looking GPR mine detection system. *Proc SPIE*. 2002;742:206–217.
8. Bradley M, Witten T, Duncan M, McCummins R. Anti-tank and side-attack mine detection with a forward-looking GPR. *Proc SPIE*. 2004;5415:421–432.
9. Wang T, Sjahputera O, Keller J, Gader P. Landmine detection using forward-looking GPR with object tracking. *Proc SPIE*. 2005;5794:1080–1088.
10. Franceschetti G, Iodice A, Riccio D. Forward-looking synthetic aperture radar (FLoSAR): the array approach. *IEEE Geoscience and Remote Sensing Letters*. 2014;11(1):303–307.
11. Richards M, Scheer J, Holm W. Principles of modern radar: basic principles. Raleigh (NC): SciTech Publishing; 2010.
12. Melvin W, Scheer J. Principles of modern radar—advanced techniques. Edison (NJ): SciTech Publishing; 2013.

13. Dogaru T, Liao D, Le C. Three-dimensional radar imaging of a building. Adelphi (MD): Army Research Laboratory (US); 2012 Dec. Report No.: ARL-TR-6295.
14. Soumekh M. Synthetic aperture radar signal processing. New York (NY): Wiley; 1999.
15. Balanis C. Advanced engineering electromagnetics. New York (NY): Wiley; 1989.
16. Liao D, Dogaru T, Sullivan A. Large-scale, full-wave-based emulation of step-frequency forward-looking radar imaging in rough terrain environments. *Sensing and Imaging: An International Journal*. 2014;15(4).
17. Nguyen L. SAR imaging technique for reduction of sidelobes and noise. *Proc SPIE*. 2009;7308.
18. Ranney K, Nguyen L, Sichina J. Iterative sidelobe reduction in transmission-constrained, stepped-frequency, synthetic aperture radar. *Proc SPIE*. 2010;7669.
19. Balanis C. Antenna theory: analysis and design. New York (NY): Wiley; 1997.
20. Ahmad F, Kassam S. Coarray analysis of the wide-band point spread function for active array imaging. *Signal Processing*. 2001;81(1):99–115.
21. Nguyen L, Soumekh M. System trade analysis for an ultra-wideband forward imaging radar. *Proc SPIE*. 2006;6230.
22. Li J, Stoica P. MIMO radar signal processing. Hoboken (NJ): Wiley; 2009.
23. Skolnik M. Introduction to radar systems. New York (NY): McGraw-Hill; 2001.
24. Carrara W, Goodman R, Majewski R. Spotlight synthetic aperture radar. Norwood (MA): Artech; 1995.
25. Jakowatz C, Wahl D, Eichel P, Ghiglia D, Thompson P. Spotlight-mode synthetic aperture radar: a signal processing approach. Boston (MA): Kluwer Academic Publishers; 1996.
26. Sheen D, McMakin D, Hall T. Three-dimensional millimeter-wave imaging for concealed weapon detection. *IEEE Transactions on Microwave Theory and Techniques*. 2001;49(9):1581–1592.

## List of Symbols, Abbreviations, and Acronyms

---

1-D	one-dimensional
2-D	two-dimensional
3-D	three-dimensional
5-G	fifth generation
ADC	analog-to-digital converter
ARL	US Army Research Laboratory
CPI	coherent processing interval
CW	continuous wave
DVE	degraded visual environment
FLSAR	forward-looking synthetic aperture radar
FMCW	frequency modulation continuous wave
GPS	Global Positioning System
IMU	inertial measurement unit
IR	infrared
LFM	linear frequency modulation
LOS	line of sight
MIMO	multiple-input multiple-output
MMW	millimeter wave
PRF	pulse repetition frequency
PSF	point spread function
PTR	point target response
RCS	radar cross section
RF	radio frequency
RMS	root mean square
RSM	recursive sidelobe minimization
Rx	receiver

SAFIRE	Spectrally Agile Frequency-Incrementing Reconfigurable
SAR	synthetic aperture radar
SIRE	Synchronous Impulse Reconstruction
SNR	signal-to-noise ratio
SWAP-C	size, weight and power, and cost
Tx	transmitter
UWB	ultra-wideband

1 DEFENSE TECHNICAL  
(PDF) INFORMATION CTR  
DTIC OCA

2 DIR ARL  
(PDF) IMAL HRA  
RECORDS MGMT  
RDRL DCL  
TECH LIB

1 GOVT PRINTG OFC  
(PDF) A MALHOTRA

9 ARL  
(PDF) RDRL SER U  
A SULLIVAN  
D LIAO  
T DOGARU  
C LE  
B PHELAN  
K SHERBONDY  
RDRL SER W  
K RANNEY  
RDRL SER M  
D WIKNER  
E ADLER